# Participation of ventricular trabeculae in neonatal cardiac regeneration leads to ectopic recruitment of Purkinje-like cells

Lucie Boulgakoff, Rachel Sturny, Veronika Olejnickova, David Sedmera, Robert G Kelly, Lucile Miquerol

# Participation of ventricular trabeculae in neonatal cardiac regeneration leads to ectopic recruitment of Purkinje-like cells

Lucie Boulgakoff[1], Rachel Sturny[1], Veronika Olejnickova[2], David Sedmera[2], Robert G. Kelly[1] and Lucile Miquerol [1]*

1- Aix-Marseille Université, CNRS UMR 7288, Developmental Biology Institute of Marseille, Campus de Luminy Case 907, CEDEX 9, 13288 Marseille, France

2- Charles University, First Faculty of Medicine, Institute of Anatomy, U Nemocnice 3, 128 00 Prague, Czech Republic

* Correspondence: Lucile Miquerol : lucile.miquerol@univ-amu.fr; Tel.: +33-413942409

Unlike adult mammals, newborn mice can regenerate a functional heart after myocardial infarction. However, the precise origin of the newly formed cardiomyocytes and whether the distal part of the conduction system - the Purkinje Fiber (PF) network - is properly formed in regenerated hearts remains unclear. Purkinje Fibers, as well as subendocardial contractile cardiomyocytes, are derived from trabeculae, transient myocardial ridges on the inner ventricular surface. Here, using Connexin40-driven genetic tracing, we uncover a substantial participation of the trabecular lineage in myocardial regeneration through dedifferentiation and proliferation. Concomitantly, regeneration disrupted Purkinje Fiber network maturation, resulting in permanent Purkinje Fiber hyperplasia and impaired ventricular conduction. Proliferation assays, genetic impairment of Purkinje Fiber recruitment, lineage tracing, and clonal analysis revealed that Purkinje Fiber network hyperplasia results from excessive recruitment of Purkinje Fibers due to increased trabecular fate plasticity. These data indicate that Purkinje fiber network hyperplasia is a consequence of trabeculae participation in myocardial regeneration.

# INTRODUCTION

In mammals, cardiac regeneration in response to ischemia is restricted to the early post-natal period due to the poor proliferative capacities of mature cardiomyocytes (CMs)[1]. In consequence, myocardial infarction (MI) at adult stages induces CM death and impaired cardiac function. Additionally, MI is followed by a high prevalence of life-threatening arrhythmias, which frequently arise from the terminal part of the ventricular conduction system: the Purkinje Fiber network[2]. This network is composed of highly specialized CMs known as Purkinje fibers (PFs), forming ellipsoid structures on the luminal surface of each ventricle. The PF network ensures the fast propagation of action potentials within the ventricles and its architecture directs the stereotypical apex-to-base contraction of the ventricles. Despite comprising less than 2% of CMs, the PF network is highly pathogenic, notably in association with other cardiac disorders. It is thus important to better understand PF network development and homeostasis, as well as its structure and function under pathological conditions for example following MI in either regenerative or non-regenerative contexts.

During embryogenesis, the growth of trabecular myocardium at the inner surface of the ventricles gives the heart a sponge-like structure (Extended Data Fig. 1). Trabeculae are characterized by expression of the fast-conducting gap junction protein Connexin 40 (Cx40, encoded by *Gja5*), which persists in the PF network of mature ventricles[3,4] (Extended Data Fig. 1). As cardiac development proceeds, common progenitor cells in trabeculae give rise to contractile CMs of the inner half of the myocardium and conductive CMs of the PF network through progressive lineage segregation[3]. An early PF commitment establishes a scaffold of the future PF network, which grows by recruitment during fetal stages, with a major Nkx2-5-dependent prenatal recruitment phase[5]. In parallel, acquisition of contractile fate coincides with progressive ventricular compaction and loss of trabecular identity and *Cx40* expression (Extended Data Fig. 1)[3,6,7]. The segregation between conductive and working lineages is complete by the first week of life in mice, concomitant with completion of ventricular compaction. Interestingly, completion of trabecular compaction in mice also coincides with the postnatal loss of regenerative capacities, while in some lower vertebrates such as zebrafish, maintenance of a trabeculated heart is associated with persistent cardiac regenerative capacities[8,9]. This raises questions as to whether 1) regeneration depends on the presence of trabecular myocardium and 2) the regenerative process interferes with the postnatal maturation of trabecular derivatives, particularly the PF network.

Using genetic tracing of trabecular derivatives during the regenerative process we reveal a substantial participation of trabeculae in the regeneration of the myocardium, through a mechanism of dedifferentiation and proliferation. In parallel, molecular, structural and functional characterization of the PF network in regenerated hearts showed that the regeneration process perturbs PF network maturation, producing a hyperplastic network composed of an excess of poorly differentiated PFs and associated with impaired ventricular conduction. Using *Nkx2-5* haploinsufficient mice, we demonstrate that hyperplasia of the Purkinje network arises from ectopic Nkx2-5-dependent recruitment of trabecular derivatives toward a conductive fate. Using clonal analysis to investigate single cell behavior following neonatal MI we found increased cell plasticity within subendocardial myocardium during cardiac regeneration. Together these data reveal that postnatal myocardial damage extends the normal time window during which conductive and working cardiomyocytes segregate within the trabecular lineage, identifying PF network hyperplasia as a cost of CM regeneration and providing new insights into the cellular and genetic basis of cardiac regeneration.

# Results

To study cardiac regeneration, we surgically induced myocardial infarction by permanent ligation of the left coronary artery in neonatal mice (P1)[10]. The ligation was validated by the visualization of the knot on the coronary artery of *Connexin40-GFP* mice, in which GFP is expressed in coronary artery endothelial cells (Fig. 1a). To identify the region of regenerated myocardium, we first quantified the extent of damage caused by neonatal MI two days post-injury (dpi). The detection of CD45-positive immune cells (Fig. 1b) showed that myocardial damage is mainly localized near the ligation point where it is transmural (n=8/11) and ventral (n=11/11). In two thirds of infarcted hearts, the affected territory extends to the apex (n=7/11) where it spreads from the ventral to the dorsal part of the heart and forms an internal crescent in the ventricular wall (n=5/11) or covers the total wall thickness (n=2/11). Three weeks after surgery, when myocardial regeneration is considered complete (Fig. 1a), only a thin internal scar remains, labeled with wheat germ agglutinin (WGA)[11] (Fig. 1b). Due to the efficient regeneration, the initially infarcted territory cannot be precisely delimitated. We thus used the remaining scar as a proxy to define a region of interest (ROI) in the ventral part of the heart, which is enriched in regenerated myocardium, and is hereafter referred to as the regenerated area. A corresponding dorsal region of equal area was considered as a control region.

## Trabecular lineage contributes to the regenerated myocardium

In order to test whether CMs that originate from the trabeculae possess enhanced regenerative capacities compared to the rest of the myocardium, we performed genetic tracing of embryonic trabeculae using *Cx40-CreERT2::R26R-YFP* mice injected with tamoxifen at E14.5 (Extended Data Fig. 1a Fig. 1c). Neonatal MI was induced at P1 and the content of labelled cells in the regenerated myocardium (MI) was compared to that of unaffected myocardium (Sham) at 21 dpi (Fig. 1c). As CMs derived from embryonic trabeculae are predominantly present in subendocardial regions (Fig. 1d)[3,7], we spatially quantified YFP+ CMs with respect to the distance from the endocardium. We designed a semi-automatic pipeline to virtually divide the ventricular wall in the ROI into 10 radial layers (L1-L10) from the endocardium to epicardium. The surface covered by YFP staining was quantified in each layer (Fig. 1d, e). Finally, to counteract the variability of recombination between individuals, the YFP area in each layer of the ROI was normalized to the total YFP area in the control region, which reflects the recombination rate. The analysis was conducted in sections throughout the affected region, from the ligation point to the apex where a remaining scar was observed.

Consistent with the reported endocardial to epicardial expression gradient of Cx40[6], the percentage of YFP+ CMs gradually decreases from the endocardium to the middle of the ventricular wall (L1 to L5) and 90% of YFP-labeled CMs were found in the 3 innermost radial layers (L1 to L3) (Fig. 1f, Extended Data Table 1). In regenerated regions, three weeks after neonatal MI, we found an increase (from 2.5 to 6.5-fold) of the YFP area in L3 to L8 (p-value <0.0001 in L3 to L6, 0.002 in L7 and 0.013 in L8) (Fig. 1f, Extended Data Table 1). This indicates that the trabecular lineage makes a significant contribution to the regenerated myocardium. In the innermost subendocardial regions (L1-2) no difference in the YFP area was found between sham and regenerated hearts, consistent with the fact that the subendocardial myocardium initially derives from, and is regenerated by, the trabecular lineage. In contrast, subepicardial outer regions (L9-10) do not contain trabecular derivatives after regeneration, implying that they have regenerated independently, likely from CMs derived from the compact layer. The embryonic trabecular lineage thus contributes significantly to regeneration of the inner half of the myocardium but is not the exclusive source of new CMs during regeneration.

At the time of birth, only the most subendocardial portion of the myocardium remains trabeculated (Extended Data Fig. 1). We next tested whether, beyond a trabecular origin, the maintenance of a trabecular fate confers enhanced regenerative potential to perinatal trabeculae compared to the rest of embryonic trabeculae and compact myocardium. We used a similar approach

as above but with an injection of 4'OH-tamoxifen at perinatal stages (E18.5) to *Cx40-CreERT2::Rosa-TdTomato* mice (Extended Data Fig. 2a) to label perinatal trabeculae. As expected, the vast majority of labeled CMs were found in the most subendocardial regions of the myocardium (L1-2) in the Sham (Extended Data Fig. 2b-c-d, Extended Data Table 1). In regenerated territories, the TdTomato area increased by 3-6-fold in L3 to L6 (p-value <0.05 in L3, L5 and L6 and <0.01 in L4) (Extended Data Fig. 2d), a similar rate to that observed for the embryonic trabecular lineage (Extended Data Table 1, Extended Data Fig. 2e-f).

Together, these data demonstrate that trabecular derivatives increase their contribution to the ventricular wall during regeneration and have similar regenerative capacities at embryonic and perinatal stages.

## MI induces trabecular cell cycle activity and dedifferentiation

The presence of trabecular derivatives in regenerated myocardium implies that cell cycle activity in the trabecular lineage occurs during myocardial regeneration after neonatal MI. To detect DNA replication in trabecular derivatives during the regeneration process, we combined genetic tracing of embryonic trabeculae, labelled by a tamoxifen injection at E14.5, with modified-nucleotide incorporation assay. As the MI-induced proliferation phase has been described to peak at 7dpi[12–14], EdU was injected into *Cx40$^{CreERT2/+}$::Rosa-YFP$^{Fl/+}$* mice at 5 and 11dpi (Fig. 2a). 21 days after MI, the proportion of YFP+ CMs that have incorporated EdU (YFP+ EdU+/ YFP+) is 30% greater in MI (9%) than in sham-operated mice (6.4%) (Fig. 2b-c) (p<0.001). This shows that increased cell cycle activity in the trabecular lineage accompanies cardiac regeneration.

Since maturation of mammalian CMs is a barrier to proliferation, we investigated whether differentiation of the trabecular lineage is delayed during the regeneration process (Fig. 2d-f). At E14.5 and P0, Cx40 is expressed in all CMs from the trabeculated myocardium[6] (Fig. 2e). Consistent with previous observations[3], contractile CMs from P6 Sham hearts had downregulated Cx40 expression compare to P0 (*Cx40-GFP*: Fig. 2f, g; endogenous Cx40 protein: Fig. 2h, j), while the innermost subendocardial CMs which are committed to a conductive fate, have upregulated Cx40 (Fig. 2h, i). However, in 5dpi MI hearts, contractile CMs of the BZ display high levels of Cx40-GFP (Fig. 2g) and endogenous Cx40 protein (Fig. 2h), even in deep subendocardial myocardium (Fig. 2i, j, white arrows), similar to E14.5 and P0 hearts (Fig. 2e). This suggests that the trabecular marker Cx40 either fails to be downregulated, or is re-expressed, during the regeneration process. Moreover, CMs from the BZ subendocardial myocardium, especially CMs expressing high levels of Cx40-GFP, exhibit low sarcomere assembly at 5dpi (Extended Data Fig. 3).

Overall, during cardiac regeneration, the trabecular lineage displays enhanced cell cycle activity, high levels of Cx40 expression and low sarcomere assembly, indicating that myocardial regeneration is associated with by the maintenance or reversion to an immature state in the trabecular lineage.

## The PF network is unable to regenerate when damaged

Neonatal mice are considered capable of cardiac regeneration since they are able to regrow an overall functional heart after MI[10,12]; however, little is known about the ability of the PF network to regenerate in this context. First, we observed that the surgically-induced MI initially affects the PF network only at the site of the ligation where a visible hole appears in the network (Fig. 1b et 3a-b). However, below the ligation point, the PF network is unaffected by the initial ischemic damage (Fig. 1b et 3b). After complete regeneration of the working myocardium (21 dpi), a hole in the PF networks persists at the level of the ligation (Fig. 1b-3b). PFs, scored using Cx40-GFP on whole-mount or Cntn2 immunofluorescence on whole mount and sections, remain absent at the ligation point while they are present in the BZ (Fig. 3c-d). Neonatal mice thus fail to repair damage to the PF network following MI.

To discriminate between incomplete or absence of PF network regeneration, we quantified the proportion of the damaged PF network on successive transverse sections. Knowing that the PF network covers the ventricular lumen – the proportion of damaged PF network was expressed as the length of affected ventricular lumen (CD45-positive at 1 to 3dpi or WGA-positive at 21dpi) over the total luminal perimeter (Fig. 3c-d). At early time points after MI, the size of the damaged PF network is small and variable, ranging from 0 to 7.1% of the ventricular lumen area with a mean of 1.7% (Fig. 3e), while no damaged PF network could be observed in Sham-operated mice (Extended Data Fig. 4). Three weeks after MI, when regeneration is considered complete, the frequency and the size of damaged PF network were similar to those after initial ischemia-induced damage (from 0 to 6.8%, with a mean of 2.1%) (Fig. 3e). No damage to the PF network was observed in Sham-operated mice at this stage (Extended Data Fig. 4). The indistinguishable extent of damage observed in the PF network after MI, before or after regeneration, confirms that the PF network, although being only minimally damaged by the MI, is unable to regenerate.

## The PF network in the border zone is hyperplastic

Knowing that the regeneration process involves wide changes in signaling cues and cellular behavior, we hypothesized that it could interfere with the maturation of the PF network in the BZ. We used Cx40 and Cntn2, known markers of mature PFs[15,16] to characterize PF network architecture following regeneration. On whole-mount LV views, we observed a global increase in Cx40-GFP and Cntn2 staining in the cardiac apex (Fig. 3f). We then semi-automatically quantified the Cntn2+ area on successive sections below the ligation point (Fig. 3g-h, Extended Data Fig. 5b) and counted the number of Cntn2-positive PFs per section (Fig. 4h-i), both normalized by the ventricular luminal perimeter. These measurements demonstrate that both the PF network area and PF number are 2-fold higher in the MI compared to the sham, defects that are still present six months after the injury (Extended Data Fig. 5c). Interestingly, hyperplasia specifically affects portions of the PF network that were in the BZ of the infarction (apical PF network, especially in the LV free wall), and not initially damaged by the MI. Overall, this data suggests that regeneration of the working myocardium interferes with normal maturation of the PF network in the BZ, resulting in the development of a permanently hyperplastic network, consistent with recent reports [17].

## The hyperplastic PF network include undifferentiated PFs

PFs are distinguishable from CMs by the specific – or enriched – expression of transcription factors, adhesion molecules, ion channels, gap junctions and by a more elongated shape. To test whether the PFs from the hyperplastic PF network of regenerated hearts possess a proper conductive phenotype, we compared the expression levels of PF-enriched genes in the PF network of regenerated and Sham hearts. We designed a panel of 84 genes reported to be PF-enriched[15,16,18–24] (Supplementary Table) and performed high-plex smFISH against these genes three weeks after neonatal MI (Fig. 4a-b). We manually segmented the PF network – as Cntn2 positive – and the contractile myocardium (Extended Data Fig. 6a). Consistent with efficient myocardial regeneration, most tested genes showed similar expression levels in the contractile myocardium of MI and Sham. In our dataset, 52 genes were enriched in the PF network vs contractile myocardium of Sham hearts including 41 genes with p-value<0.05 (Fig. 4c, Extended Data Fig. 6b). In Sham hearts, PF-enriched genes are expressed at high and homogenous levels in PFs and at low and sparse levels in contractile CMs (Fig. 4b, d-f). Strikingly, 47 of the 52 PF-enriched genes were downregulated in the hyperplastic PF network of regenerated compared to Sham hearts including 37 genes with p-value<0.05 (Fig. 4c, Extended Data Fig. 6b). This includes genes encoding well-known transcription factors regulating conductive-fate such as Etv1, Irx3, Nkx2-5 and Tbx5 as well as gap junctions and ion channels essential for conduction, including Cx40, Hcn4 and Cacna2d2. Only 4 PF-enriched genes (7.7%) were expressed at physiological levels in the hyperplastic PF network after MI, and only *Nppa* was up-regulated compared to the Sham (p-

value=0.002) (Fig. 4f, Extended Data Fig. 6b). Moreover, the expression level of conductive genes is heterogenous among PFs of the hyperplastic PF network (Fig. 4b, d-f). Indeed, Cntn2 expression extends to the subendocardial territory in sheets of cells with a graded level of expression at both 21dpi or 6mpi (Fig. 4d, Extended Data Fig. 5d). Likewise, the expression levels of Hcn4 and Sema3a are heterogenous among Cntn2+ cells ranging from no expression to levels similar to Sham hearts (Fig. 4e-f). Moreover, contrary to Sham hearts where the PFs are organized in well-defined fascicles, Cntn2-positive cells form poorly defined sheets. Thus, the hyperplastic PF network of regenerated hearts has an intermediate transcriptional phenotype between a normal PF cells and contractile myocardium.

Next, we compared PF shape in sham and regenerated heats. To identify single PFs in three-dimensions, we induced sparse cell labelling by crossing the *R26R-Confetti* reporter mice with *Mesp1-Cre* (Fig. 4g), and labelled PFs by Cntn2 staining on whole-mount opened ventricles (Fig. 4h). In contrast to sham-operated hearts, numerous short and wide PFs were observed in the hyperplastic PF network (Fig. 4h-i). Overall, the median length-to-width ratio of PFs was 34% lower in MI than Sham (Sham= 8.5, MI= 5.6, p-value< 2,2e-16) (Fig. 4i), showing that cells comprising the hyperplastic PF network fail to adopt the stereotypical elongated shape of differentiated PFs.

Together, analysis of expression levels of transcription factors, gap junctions, cell adhesion molecules, ion channels as well as cell shape show that the hyperplastic PF network of regenerated hearts fails to adopt a normal conductive phenotype, and rather displays a signature intermediate between contractile myocardium and PF network.

## Perturbed electrical propagation in hyperplastic PF network

Given the perturbed structure and transcriptional profile of the hyperplastic PF network of regenerated hearts, we next asked whether its conductive properties were affected (Fig. 5a).

We first analysed the fast conducting gap junctions Cx40 and Cx43, which are respectively responsible for fast conduction in the PF network and contractile myocardium. Consistent with the results of our transcriptional analysis, we observed decreased and heterogenous expression of Cx40 within the PF network of MI (Cntn2 positive cells), ranging from no expression to similar levels to those in Sham hearts (Fig. 5b, Extended Data Fig.5d). Although the content of Cx43 was similar in the PF network of MI and Sham hearts (Fig. 5c), whole-mount staining for Cx43 revealed a heterogenous distribution of Cx43 junctions in the hyperplastic PF network (Fig. 5c), likely inadequate to ensure fast and directional conduction in the hyperplastic PF network of MI.

In order to test electrical propagation in regenerated heats, we performed electrocardiogram recordings on 21 dpi mice (Fig. 5d). The QRS interval increased by 12% in MI compared to the sham hearts (Fig. 5e, Extended Data Fig 5e), indicating a slower AP propagation in the ventricles following MI. Moreover, the angle of the main activation axis was highly variable (Fig. 5f), though remaining in a normal range (0 to 120°), showing that the stereotypical depolarization pattern is slightly affected in regenerated hearts.

In an attempt to distinguish whether this slower ventricular conduction results from the small residual scar, from defective conduction within the contractile myocardium or from the abnormal PF network, we performed epicardial and endocardial optical mappings. Epicardial activation maps show normal activation pattern in regenerated hearts, showing that the residual scar does not measurably perturb electrical conduction (Fig. 5g and Supplementary Movies 1 and 2). Similarly, endocardial activation maps show septal activation starting from half-septal height in both Sham and MI, with similar conduction velocity in both cases (Fig. 5g and Supplementary Movies 3 and 4). However, this approach does not allow us to record activation from the PF network alone. Overall, this functional

study uncovers mild conductive defects in regenerated hearts, demonstrating that myocardial repair is incomplete with respect to cardiac conduction.

## Impairing PF recruitment prevents MI-induced PF hyperplasia

We reasoned that the excess of PFs found in regenerated hearts may arise from either an increased proliferation of PFs, or an excessive recruitment of cells toward a conductive fate following MI. To discriminate between these two mechanisms, we first compared the proliferation within the PF network of Sham or MI-operated mice (Fig. 6a). We subjected mice to a neonatal MI, injected them with EdU at 5 and 11dpi and, three weeks after the surgery, we found similar levels of EdU incorporation in the PF network of Sham and MI operated mice (Fig. 6b-c), which strongly suggest that hyperplasia of the PF network do not result from excessive proliferation of preexisting PFs.

Next, to investigate whether PF network hyperplasia results from excessive recruitment of PFs, we performed MI in a mouse model with genetically impaired PF recruitment (Fig. 6d). At late fetal stages, the recruitment toward a conductive fate requires maximal levels of the transcription factor Nkx2-5, while Nkx2-5 levels have no impact on PF proliferation[5]. We subjected *Nkx2-5$^{LacZ/+}$* mice to a neonatal MI and compared their PF network volume in response to MI with that of *Nkx2-5$^{LacZ/+}$* Sham mice. Strikingly, the PF network of *Nkx2-5$^{LacZ/+}$* MI-operated mice did not increase in volume after regeneration, compared to *Nkx2-5$^{LacZ/+}$* Sham-operated mice, and was thus still hypoplastic after regeneration (Fig. 6e-f). This shows that the excessive PF production during the regenerative process, which leads to PF network hyperplasia in WT, relies on maximal levels of Nkx2-5. This similarity with the perinatal recruitment of PFs strongly suggests that excessive PFs produced during regeneration arise by excessive recruitment.

As previously described, electrocardiograms reveal that *Nkx2-5$^{LacZ/+}$* Sham mice have an increased QRS duration compared to Sham WT mice and this defect has been attributed to the hypoplastic PF network (Fig. 6g, Sham)[25,26]. *Nkx2-5$^{LacZ/+}$* mice, unlike WT mice, do not develop further QRS defects in response to MI, consistent with the similar PF network architecture in sham versus MI-operated *Nkx2-5$^{LacZ/+}$* mice (Fig. 6g).

Overall, these results strongly suggest that the excess PFs found in regenerated WT hearts are produced by excessive PF recruitment rather than by proliferation of preexisting PFs.

## MI-induced PFs derive from perinatal trabeculae

Cells that are recruited to a conductive phenotype are thought to originate from trabecular cells of the subendocardial myocardium at late fetal stages[3,5]. To test whether this is also the case during regeneration following neonatal MI, we labelled subendocardial cells by a 4-hydroxy-tamoxifen injection to *Cx40-CreERT2; R26R-tdTomato* mice at E18.5 (Fig. 7a). The percentage of labelled cells in the remote PF network was variable between individual hearts due to recombination efficiency, ranging from 25 to 60% (Fig. 7b-c). However, paired-analysis showed no difference in the proportion of labelled cells in the hyperplastic PF network compared to the remote. This confirms that the hyperplastic PF network is derived from subendocardial myocardium.

## The regenerative process prolongs trabecular plasticity

At birth most CMs are already committed to either conductive (PF) or contractile fates, and only a very low proportion of cells retains bipotency in subendocardial regions[5]. Contractile and conductive CMs start to diverge molecularly, as seen by the onset of Cntn2 expression in the earliest differentiating PFs, and downregulation of Cx40 in contractile CMs (Fig. 8a). Thus, from birth, high expression of Cx40 is mainly limited to fascicles of the prospective PF network.

We hypothesized that an increased plasticity between contractile and conductive lineages in subendocardial regions may underlie PF network hyperplasia in response to MI. Additionally, we hypothesized that CMs could retain or recover proliferative and bipotent capacities, and thus participate in both myocardial regeneration and PF network hyperplasia. We performed a retrospective clonal analysis of subendocardial cells at the time of the surgery, in order to study their proliferation and fate during regeneration (Fig. 8a). Individual cells expressing Cx40 were labelled by the injection of a low dose of 4-hydroxy-tamoxifen to *Cx40-CreERT2::R26R-Confetti* mice at P1. Three weeks post-surgery, individual clones derived from a unique labeled cell were identified in whole-mount hearts and on serial sections. Based on the level of Cntn2 expression (high, null or low) each cell within individual clones was scored as PF, working CM or intermediate. Accordingly, the clone was classified in one of three categories: conductive, if composed only of PFs, contractile if composed of only of working CMs, and mixed when containing intermediate cells or a combination of cell types (Fig. 8b). Clone size, i.e. the number of labelled cells per clone was also scored.

In Sham operated hearts, the vast majority of clones (83%) were conductive, consistent with Cx40 expression being largely restricted to committed PFs at P1 (Fig. 8c, Extended Data Table 2a). However, in regenerating hearts after MI, fate choices were much more balanced between the different type of clones. Indeed, contractile clones represent 30% of clones in MI compared to 11% in Sham hearts (p-value: 0.004). Similarly, while the proportion of mixed clones – revealing bipotency of the mother cell – was very low in the sham (5%), mixed clones were 4-fold more frequent after MI (21% in MI hearts, p-value: 0.004), with a similar increase of each sub-categories of mixed clones (Fig. 8c-d, Extended Data Table 2a-b). Together, increased contractile fate and recovery of bipotency show increased fate plasticity of Cx40-P1 cells during the regenerative context, reminiscent of earlier developmental stages[5].

Interestingly, mixed clones were found to be larger than conductive or contractile clones, in both MI and Sham (Cells per clones in the MI: Mixed clones: 3.23, contractile clones: 1.98 and conductive clones: 1.78) (Fig. 8e, Extended Data Table 2b), showing that bipotency is accompanied by increased proliferation in subendocardial cells. Overall, the reacquisition of bipotency after MI, combined with superior proliferative capacities of bipotent cells, allows for a 22% increase in the number of daughter cells generated by subendocardial cells (Sham = 174, MI =210 daughter cells per 100 mother cells, p-value= 0.017) (Fig. 8f, Extended Data Table 2c).

Next, to test the proliferation capacities of PFs in response to MI, we counted the number of cells in conductive clones. Each conductive clone was composed of one to three PFs, with no difference between MI and Sham (Sham: 1.70, MI: 1.78, $p_{wilcox\ (Sh\ vs\ MI)}$ =0.4) (Fig. 8e, Extended Data Table 2a), showing no increase in the proliferation of PFs in response to MI. This further confirms that MI-induced hyperplasia results from increased PF recruitment rather than PF proliferation.

Surprisingly, Cx40-P1 mother cells generate a similar number of daughter cells with conductive properties (PFs + intermediate cells) in MI compared to Sham (Sham = 151, MI =137 PFs + intermediate daughter cells per 100 mother cells, p-value= 0.18) (Fig. 8f, Extended Data Table 2c). This suggest that Cx40-P1 cells are not responsible for PF network hyperplasia. Therefore, ectopic PFs after MI arise from the recruitment of CMs in the subendocardial territory (cartoon from Fig 8a shows Cx40-P1 cells), nonetheless derived from perinatal trabeculae (cartoon from Fig. 6a shows perinatal trabeculae).

# Discussion:

Our lineage tracing approach uncovered a significant contribution of the trabecular lineage to myocardial regeneration following neonatal MI. Thus, despite their early differentiation onset and low proliferative capacities during development[27–29], trabecular derivatives retain regenerative capacities postnatally. Consistently, the great difference between proliferation rates in compact and trabecular myocardium observed at early time points reduces during late fetal development[28], is no longer observable at P7[7] and inversed at adult stages[30]. We found that derivatives of embryonic trabeculae, a proportion of which is compacted a birth, contribute in the same manner to the regenerated myocardium than perinatal trabeculae. This implies that regenerative capacities within the trabecular lineage does not depend on the state of compaction at the time of regeneration, nor on the distance to the endocardium. We were unable to directly compare the regenerative abilities of trabecular and compact CMs because of experimental limitations - non-uniform and limited labeling of trabeculae by the Cx40-driven Cre and absence of lineage tracing of the compact layer. Nonetheless, our results shows that trabecular derivatives contribute significantly to regenerate myocardium although they do not massively participate in the regeneration of subepicardial layers as they do in zebrafish[31]. Overall, our lineage tracing approach does not identify major spatial heterogeneity in regenerative capacity at tissue scale, although it does exist at the cellular level[32–35].

During regeneration we found an immature trabecular identity at the BZ, which could reflect a delay of differentiation or a dedifferentiation of the trabecular lineage. These data are consistent with the extensively described dedifferentiation of CMs during cardiac regeneration, including sarcomeric disassembly, expression of embryonic actin and metabolic changes[12,32,36–43]. It is interesting to note that trabecular markers are also re-expressed after adult MI in the BZ[44,45] although it is insufficient to promote cardiac regeneration in this context.

We observed that, except for local damage at the site of the ligation, the PF network is largely preserved after neonatal MI consistent with reports in dogs[46], pigs[47] and neonatal piglets[48]. However, after regeneration, we found: 1) local defects at the site of the ligation, directly resulting from the ischemic damage and attesting that the PF network is incapable of regenerating 2) overall hyperplasia of the PF network arising in the BZ as secondary defect of the regeneration process. These data support and extend recent evidence for PF hyperplasia following neonatal MI[17] and confirm that PFs are not regenerative, even in newborn mice, despite remaining diploid[49]. Our results confirm and extend an earlier report of PF network hyperplasia post-MI [17] by showing that MI-induced PF network hyperplasia results from ectopic recruitment of PFs. Recruited cells arise from perinatal trabeculae, in a process reminiscent of late fetal PF recruitment[5], which depends on maximal levels of Nkx2-5.

Interestingly, our data reveal increased plasticity between contractile and conductive fates within the trabecular lineage in response to neonatal MI, a property reminiscent of earlier development stages[5]. However, in the hyperplastic PF network, a significant proportion of cells permanently displays an intermediate phenotype between contractile CMs and PFs, indicative of an incomplete conductive maturation. Similarly, overactivation of the Notch pathway [50] results in the production of an hyperplastic PF network, composed of cells with an intermediate phenotype both at the molecular and electrophysiological levels. This attests to postnatal plasticity of subendocardial CMs under certain conditions, and raises the question of whether the failure of complete conversion to PF results from insufficient plasticity in the neonatal period or from aberrant signals. Recently, scRNA seq analysis has highlighted a intermediate transcriptome between PFs and working CMs during development[20]. Though these cells were proposed to represent transitional cells of the Purkinje-to-myocardium junctions, they may rather identify an intermediate developmental state observed at early time points.

Characterization of electrical conduction uncovers a reduction of ventricular conduction velocity in regenerated hearts, arguing that cardiac regeneration does not produce a fully functional heart as previously suggested based on echocardiography[10,51–53]. Similar to our findings, a clinical report of a patient who experienced a neonatal MI uncovered slight conduction defects despite recovery of most cardiac functions[54]. Our optical mapping experiments did not identify major disturbance around the remaining scar but could not confirm that conduction defects arise from the abnormal PF network of regenerated hearts. Although the lengthening of the QRS duration in regenerated mice hearts was mild, it could progress, with time or under stress conditions, to more severe conductive defects or arrythmia, as observed with *Nkx2-5* postnatal deficiency[55]. Moreover, it is a common observation that murine models of cardiomyopathy, although closely reproducing molecular or structural defects observed in human, develop milder functional defects than human patients suffering from the corresponding cardiomyopathies [55,56]. Thus, given the strong structural and molecular defects of the PF network of regenerated hearts, potential functional defects in human should not be underestimated due to the mild conduction defects observed in mice.

Increased PF network volume, abnormal molecular and decreased conductivity was also reported in adult mammals after congestive heart failure[57] or increased over-load[58]. However, this result from a hypertrophic rather than hyperplastic remodeling of the PF network.

To conclude, our data shows that neonatal regeneration, though restoring cardiac form and contractile function[53,59] is nonetheless incapable of producing a fully normal heart with respect to the ventricular conductive system. We present the first evidence for dedifferentiation and plasticity within the trabecular lineage during cardiac regeneration. Indeed, participation of the trabecular lineage in the regeneration of the working myocardium is coupled with excessive production of poorly differentiated PFs which likely participate in perturbed electrical conduction (Extended Data Fig. 7). Together, our results suggest that conduction system defects are a detrimental consequence of prolonged contribution of the trabecular lineage to regenerating myocardium.

# Materials and Methods

## Ethic statement

All studies and procedures involving animals were in strict accordance with the recommendations of the European Community Directive (2010/63/UE) for the protection of vertebrate animals used for experimental and other scientific purposes. The project was specifically approved by the ethics committee of the IBDM SBEA and by the French Ministry of Research (APAFIS #16221-2018072015086233 v2). Husbandry, supply of animals, as well as maintenance and care of the animals in the Animal Facility of CNRS-IBDM (facility license #G-13 055 21) before and during experiments fully satisfied the animals' needs and welfare.

## Mouse lines

The *Cx40-CreERT2* [60], *Cx40-GFP* [4], *R26R-YFP* [61], *R26R-TdTomato* [62], *R26R-Confetti* [63] , *Mesp1-Cre* [64] and *Nkx2-5$^{LacZ}$* [65] mouse lines have been previously reported. Mice were housed at room temperature of 22±3°C, at a relative humidity between 45% and 65% and light:dark cycle of 12/12h.

## Tamoxifen injection

For genetic tracing analysis at E14.5, *Cx40-CreERT2* males were crossed with *R26R-YFP* females and tamoxifen (150µl) was injected intraperitoneally to pregnant females. Tamoxifen (T5648, Sigma) and progesterone (P-3972-5g, Sigma) were dissolved at the concentration of 20mg$ml^{-1}$ an 10mg.$mL^{-1}$ respectively in sunflower oil. Newborn mice were recovered after caesarian and given for adoption to CD1 females.

For genetic tracing analysis at E18.5, *Cx40-CreERT2* males were crossed with *R26R-TdTomato* females and 4-Hydroxytamoxifen (4-OHT H6278, Sigma) was injected to pregnant females. 4-OHT was dissolved at the concentration of 10 mg. $ml^{-1}$ in ethanol/Cremophor® EL (Sigma) solution (50:50). Before injection, 4-OHT was diluted at the concentration of 3 mg.$ml^{-1}$ in 1× PBS and 200 µl to 250µL of this solution was injected intraperitoneally into pregnant females.

For clonal analysis, *Cx40-CreERT2*; *R26R-Confetti* pups were injected with 4-Hydroxytamoxifen at P1. 4-OHT was dissolved at the concentration of 10 mg. $ml^{-1}$ in ethanol/Cremophor solution (50:50). Before injection, 4-OHT was diluted at the concentration of 0.5 mg.$ml^{-1}$ in 1× PBS and 25µL of this solution was injected intraperitoneally into pups.

Surgery

Myocardial infarction was induced surgically at P1 on mice by permanent ligation of the left anterior descending artery as previously described [10]. Following analgesia with buprenorphine (0.05mg/kg), neonates were briefly sedated with isoflurane induction (chamber 5% isoflurane) followed by hypothermia-induced anesthesia on ice (4min). Neonates were then placed on an ice pad for surgery. Skin was incised, pectorals major et minor muscles were sectioned and the thorax opened in the 4th intercostal space. The left anterior descending artery was ligated just below the atria with non-resorbable 10-0 Ethilon (FG2820, Ethicon). Thorax and skin were closed with a resorbable 8-0 vicryl (ref V548G, Ethicon). Finally, neonates were reanimated at 37°C.

Edu injection

A solution of 5mg/mL of EdU (Baseclick, BCN-001-50) was injected intraperitoneally in mice at P6 and P12 at a dose of 25 and 20mg/kg respectively.

Surface electrocardiography

Surface ECGs were performed on anesthetized mice. An induction with 5% isoflurane was followed by maintenance at 1 to 2% in a constant flow of oxygen at 700 ml/min. ECGs were recorded three weeks after the surgery with a bipolar system in which the electrodes were placed subcutaneously at the right (negative) and left forelimb (reference) and the left hindlimb (positive) for lead II, at the right (reference) and left forelimb (negative) for lead III. Electrodes were connected to a Bioamp amplifier (AD Instruments) and were digitalized through an A/D converter ML 825 PowerLab 2/25 (AD Instruments). Digital recordings were analyzed with LabChart software version 8.1.13 (AD Instruments). Events were registered to 100 K/s and were filtered to 50 Hz. ECG recordings were obtained for 1 min after stabilization of the signal.

Antibodies

Antibodies used in this study are specific to, Anti-α-Actinin (Sarcomeric) made in Mouse (1:500, product A7732, Sigma Aldrich), GFP made in chick (1:500; 2010, Aves), Cx40 and Cx43 homemade in Rabbit [6], Contactin-2 in Goat (1:100; AF1714 R&D Systems, Minneapolis, MN, USA), monoclonal CD45 antibody in Rat (1:500; Product # 14-0451-82, eBioscience)

Secondary antibodies: Donkey anti-Mouse AlexaFluor-568 (1:250; A10037, Life Technologies), Donkey anti-goat-647 (1:250; A21447, Life technologies), Donkey anti-chick-488 (1:250; 703 545 155, Interchim), Donkey anti-chick-647 (1:250; 703 605 155, Jackson ImmunoResearch), and Donkey anti-Rat 647nm (1:250; 712 605 153, Jackson ImmunoResearch)

WGA-555 (1:500; Wheat germ agglutinin, 29076-1, Clinisciences), WGA-647 (1:500; Wheat germ agglutinin, 29024-1, Clinisciences).

Histology

To obtain full diastole, mice received an intraperitoneal injection of 10µL/g of heparin before cervical dislocation. Hearts were then dissected out and PBS-KCl (50mM) was immediately retro perfused by the aorta. Global external views were directly acquired with a Zeiss Axio Zoom.V16 to validate the correct position of the ligation on the artery. In the case of open ventricles studies, atria were cut off, left free-ventricular wall was cut open from the basis to the apex between papillary muscles and hearts were pinned flat on a petri dish. Hearts were then fixed in 4% paraformaldehyde (15714 Electron Microscopy

Sciences) overnight at 4°C, washed in PBS. Cryoprotection was achieved by successive baths of sucrose 15%, 30% and OCT (VWR Chemicals ref. 361603E) from 12 to 24h each, followed by freezing in OCT on dry ice and storage at -80°C before sectioning.

In the case of sections studies, hearts were cryosectioned at a thickness of 12µm for newborn stages (P3-P5) and 20µm for later stages (P22). Sections were preserved at -80°C before immunostaining.

EdU revelation

For EdU revelation, sections were permeabilized for 2H at RT in gelatin buffer (0.2% gelatin, 0.5% Triton, 0.1% Saponin). After PBS washes, the EdU reaction was performed for 30min at RT in a solution containing 0.1M of Tris pH7, 4mM of CUSO4, 1µM of Cyanine 3 (Baseclick BCFA-080-1), 0.1M of L-ascorbic acid. Sections were then washed in gelatin buffer and further processed with a classic immunofluorescence, as stated bellow.

Immunofluorescence

Sections were permeabilized for 20min (PBS 1×/0.2% Triton X100) and blocked for 1h (PBS 1×/3% bovine serum albumin/0.1% Triton X100/0.05% Saponin). The primary antibodies and WGA were incubated in blocking buffer for overnight at 4°C. Secondary antibodies coupled to fluorescent molecules were incubated in blocking buffer for 1h. After washes sections were mounted with DAPI-fluoromount (Ref 010-20 Southern Biotech).

For wholemount immunofluorescence, hearts were permeabilized for 1h (PBS 1×/0.5% Triton X100) and blocked ON (PBS 1×/5% bovine serum albumin/0.1% Triton X100). The primary antibodies were incubated in blocking buffer for 3 days at 4°C, followed by 2 days of PBS 1x/0.1 Triton X100 washes. Secondary antibodies coupled to fluorescent molecules were incubated in blocking buffer 3 days followed by 2 days of washes.

RNAscope:

Fixed frozen sections - cryosectionned at a thickness of 10µm – were subjected to the RNA-scope multiplex kit v2 (TSA) for fixed frozen sections (Advanced Cell Diagnostics (ACD)). Briefly, sections were air dried at -20°C for 1 hour, washed in PBS1X, covered by hydrogen peroxide (ACD, Ref 322335) for 10 minutes, wash in $H_20$. Sections were immerged in Target retrieval (ACD, Ref 322000) for 5 minutes at 100°C, rinsed in H20 and transferred in EtOH 100%. Sections were then treated with protease III (Ref 322337, ACD) for 30 minutes at 40°C and rinsed in H20. C1-C2 and/or C3-probes were simultaneously hybridized at 40°C for 2 hours. ). Following probes hybridization, 2x2 minutes washes in RNAscope Wash Buffer (Ref 310091, ACD) were perform between each step. Amplification was performed at 40°C by sequential incubation of Amp1 (30 minutes, Ref 323101, ACD), Amp2 (30 minutes, Ref 323102, ACD) and Amp3 (15 minutes, Ref 323103, ACD) sequentially. Each probe was then revealed sequentially by a 15 minutes v2-HRP treatment specific of the corresponding channel (v2-HRP-C1: Ref 323104, v2-HRP-C2: Ref 323105, v2-HRP-C3: Ref 323106, ACD) followed by TSA-fluorophore incubation, at 40°C. The HRP was inhibited by a 15-minutes v2-HRP-blocker treatment at 40°C (Ref 323107, ACD) before revelation of the next channel. Sections were counterstained with Dapi (Ref 3204454, ACD), and finally mounted in Prolong gold antifade mountant (Ref P36934, Invitrogen).

*Probes:* Mm-Nppa-C3 (Ref 418691-C3, ACD), EGFP-C3 (Ref 400281-C3, ACD), Mm-Sema3a-O1 (Ref 433521, ACD), HCN4 (Ref 421271-C1, ACD).

*TSA-fluorophores:* TSA-Cy3 (1:1500, FP1170, PerkinElmer); TSA-Cy5 (1:1000, TS-000203, Akoya Biosciences), diluted in RNAscope Multiplex TSA Buffer (Ref 322809, Advanced Cell Diagnostics)

Molecular Cartography™

*Tissue sections:*

10µm cryosections were positioned on Resolve Biosciences slides and fixed with 4% v/v Formaldehyde (Sigma-Aldrich F8775) in 1x PBS for 5 min at 4 °C and washed 3x in 1x PBS for 1 min, followed by 1 min washes in 70% Ethanol, Isopropanol, 95% Ethanol and 70% Ethanol. 100-plex combinatorial single molecule fluorescence in-situ hybridization (Molecular Cartography™) was performed. Slides were

incubated in DST1 buffer (Molecular Cartography) and tissues prehybridized for 30 mins at 37°C prior to 24 hr hybridization with probes designed using Resolve's proprietary design algorithm (probes are listed in Supplementary Table 1). Slides were then washed and fluorescently tagged in a two-step revelation process (Molecular Cartography™) and regions of interest imaged on a Zeiss Celldiscoverer 7 using a CD7 CMOS camera (Zeiss Axiocam Mono 712).

*Probe Design:*

The probes for 100 genes were designed using Resolve's proprietary design algorithm. Briefly, the probe-design was performed at the gene-level. For every targeted gene all full-length protein coding transcript sequence from the ENSEMBL database were used as design targets if the isoform had the GENCODE annotation tag 'basic'[66,67]. To speed up the process, the calculation of computationally expensive parts, especially the off-target searches, the selection of probe sequences was not performed randomly, but limited to sequences with high success rates. To filter highly repetitive regions, the abundance of k-mers was obtained from the background transcriptome using Jellyfish[68]. Every target sequence was scanned once for all k-mers, and those regions with rare k-mers were preferred as seeds for full probe design. A probe candidate was generated by extending a seed sequence until a certain target stability was reached. A set of simple rules was applied to discard sequences that were found experimentally to cause problems. After these fast screens, every kept probe candidate was mapped to the background transcriptome using ThermonucleotideBLAST [69] and probes with stable off-target hits were discarded. Specific probes were then scored based on the number of on-target matches (isoforms), which were weighted by their associated APPRIS level [70], favoring principal isoforms over others. A bonus was added if the binding-site was inside the protein-coding region. From the pool of accepted probes, the final set was composed by greedily picking the highest scoring probes.

*Imaging:*

Excitation time per image was 1000 ms for each channel. Fluorescent signals were removed and revelation, imaging and removal of fluorescence repeated for multiple cycles for every target gene. Images were corrected for background fluorescence and signal quantitfication performed by Resolve Biosciences to spatially map transcript distributions [71].

*Downstream Analysis:*

Final image analysis was performed in ImageJ using the Polylux tool plugin from Resolve BioSciences to examine specific Molecular Cartography™ signals.

Optical Mapping:

Mice were intraperitonealy injected with heparin (100 IU, Zentiva) 5 minutes before cervical dislocation. Hearts were rapidly dissected out, connected to the horizontal Langendorff perfusion (oxygenated Tyrodes solution: NaCl 145 mmol.$L^{-1}$, KCl 5.9 mmol.$L^{-1}$, CaCl2 1.1 mmol.$L^{-1}$, MgCl2 1.2 mmol.$L^{-1}$, glucose 11 mmol.$L^{-1}$, HEPES 5 mmol.$L^{-1}$; pH = 7.4), stained with di-4-ANEPPS for 5-7 minutes (Invitrogen #D1199, 30 µl of 2.6 mM in DMSO; based on the weight proportions of the 21 dpi mice we reduced di-4-ANEPPS used in the adult mice –[72] to one third), and injected with blebbistatin for 5-7 minutes (MedChem #HY-13813, 8 µl of 29 mM in DMSO; one third of dose used in the adult mice) to minimize the motion artifact. Spontaneous left ventricular epicardial activation pattern was recorded with the Ultima L CMOS camera using a 1.6x objective and 1.0x projective Leica lens on a THT mesoscope (SciMedia, Japan) and green LED excitation and wide green filter set. To obtain the endocardial activation pattern, the left ventricle was cut open along the dorsal septum and flattened by pinning it down. Mapping was then performed as described above. Activation maps were generated using the bundled software BV_ANA. The endocardial activation maps were manually cropped to remove the activation of the cut myocardium, and to display only the activation of the subendocardial myocardium. Corresponding Cx40-GFP images of open ventricles were captured using a confocal microscope with a 2x objective after tissue transparency was enhanced by the CUBIC 2 protocol [73]. Maximum intensity projections of series of 25

to 40 sections 50 microns are displayed. Autofluorescence of the myocardium – displayed in magenta – was imaged by the excitation with the green (543 nm) laser.

Imaging and analysis

Imaging data were acquired under a Zeiss Axioimager Z1 APO1.2 for sections, under a Zeiss Axio Zoom.V16 to visualized brightfield and endogenous florescence on whole hearts and under a Zeiss LSM780 confocal microscope for wholemount immunofluorescences.

Acquisitions were made using Zeiss software Zen Blue version 3.1. Image processing and analysis was made using Zen, Image J 1.53c and Imaris software. Panels figures and schemes were made using Adobe Photoshop 21.0.2 and Adobe Illustrator 24.0.2.

Statistics and reproducibility:

All measurements were taken from distinct samples. No data were excluded from the analyses. Statistics and graphs were generated using R software (version 3.6.2) and RStudio (version 2022.02.3+492). Before conducting the Student's t-test, normality tests were carried out, if rejected or if the sample size was too small, the Wilcoxon's test was utilized instead. Wilcoxon signed-rank test was used for paired analysis. In Box plots, center line represents the, box limits represent the upper and lower quartiles, whiskers extend to 1.5x interquartile range.

All immunofluorescent and RNAscope analyses were repeated on a minimum of three samples.

Repartition of YFP or TdTomato cardiomyocytes:

A semi-automatic pipeline was designed using ImageJ to quantify the repartition of labelled CMs (Tdtomato or YFP) in the myocardial wall. ROI, control regions, endocardium and epicardium were delineated by hand. If any, endothelial cells were identified thanks to their shape and colabelling by WGA, and were manually removed. Following a gaussian blur, threshold was set manually. On the thresholded image, CMs (or clusters of CMs) were individualized using the "analyze particle" function from ImageJ. The area of each clusters and its distance to the endocardium (relative to myocardial wall thickness) were obtained in both ROI and control regions.

The YFP (or Tdtomato) area in ROI was plotted as a function of the distance to the endocardium, after normalization by the total YFP area present in control region. A step of 10% of myocardial wall thickness was used, which correspond to the radial layer described in fig2 and 3. Experiments were performed in biological replicates as stated in the figure legend. Statistical analysis to compare differences between groups used ordinary student test. Statistics and graphs were generated using R software.

Gap in the PF network:

Successive sections with an interval of 140µm were imaged from the base to the apex of the heart. On each section 1) the total ventricular lumen perimeter was delimitated semi automatically on ImageJ by manual thresholding of the fluorescent background after a 5µm gaussian blur 2) the length of damaged ventricular lumen was manually measured as the length of the lumen surrounded by CD45 labelling (1 to 3dpi) or WGA (21dpi), reflecting PF-network damages. 3) The proportion of damaged ventricular lumen was calculated from 1) and 2) for each section. Finally, each section were summed to give the percentage of damaged ventricular lumen at the whole heart level (FIGURE).

PF network density:

PF network density was measured as the Cntn2-positive area on successive transverse section, normalized by the ventricular lumen perimeter. Measures were taken from the ligation to the apex, with an interval of 140µm. Cntn2 area was measure semi automatically on ImageJ by manual thresholding following a gaussian blur of 2µm. The ventricular lumen was delimitated semi automatically on ImageJ by manual thresholding of the fluorescent background after a 5µm gaussian blur.

PF shape:

PF length and width were measured on 3D images, on Imaris software. Cntn2-immunolabelling, which localize mainly at the cellular junction, together with the mosaic labelling of CM in *Rosa-Confetti::Mesp1-CreERT2* mice, allowed, on the 3D images to identify individual PFs. Cells that couldn't be reliably individualized were excluded from the analysis. On Figure 4g MIP images are shown. On Imaris software, all PFs which could be reliably individualized were manually segmented. The RFP channel relative to each of these PFs is shown in false-color on the right panel.

Clonal reconstitution:

Clones were first identified on whole-mount open left ventricles under a Zeiss Axio Zoom.V16. Cellular resolution and conductive vs contractile phenotyping was performed on successive transverse sections, thanks to Cntn2 immunolabelling, after imaging with a Zeiss Axioimager Z1 APO1.2 (20x). To minimize variability and biased, this scoring was performed independently by two researchers blinded for condition. While there were occasional discrepancies in cell classification, particularly in the border zone in MI, it never affected the clone type, which was consistently identified as mixed by both individuals in such cases.

## Data availability:

All data supporting the findings of this study are found within the manuscript and its Supplementary Information, and are available from the corresponding author on reasonable request. Single molecule FISH data are available from Zenodo (https://doi.org/10.5281/zenodo.12773891). Source data are provided with this paper.

## Code availability:

All codes used in this study are available from the corresponding author on reasonable request.

**Acknowledgments**: We thank Nathalie Lalevée (Aix-Marseille University, INSERM UMR 1263, C2VN) and Bastiaan J. Boukens (Department of Physiology, University Maastricht, Maastricht University Medical Center) for the help in setting up and analyzing the ECGs, the Turing Centre for Living systems, for financing formations and providing a rich scientific environment. The France-BioImaging infrastructure is supported by the ANR (ANR-10-INBS-04-01, "Investissements d'Avenir"). This work was supported by the Centre National de la Recherche Scientifique (CNRS) (LM), and Institut National de la Santé et de la Recherche Médicale INSERM (RGK), by grants from the Association Française contre les Myopathies (AFM) (LM), and from the Agence nationale de la recherche (ANR) "PurkinjeNet" (LM). LB is recipient of a doctoral fellowship from the Ecole Normale Superieure (ENS) and of a doctoral fellowship extension from the Institut Marseille Maladies Rares (MarMaRa). The funders had no role in study design, data collection and analysis, decision to publish or preparation of the manuscript.

## Author Contributions Statement

L.B., L.M. conceived the project and designed the experiments; L.B. performed all experiments, image acquisition and data curation with the help of R.S. for surgical procedure; V.O. and D.S. performed optical mapping experiments; L.B. performed the statistical analysis. R.G.K. and L.M. provided funding; R.G.K. reviewed and edited the manuscript; L.B. and L.M. wrote the manuscript.

## Competing Interests Statement

The authors declare no competing interests.

## Figure Legends

**Fig. 1: Cardiomyocytes derived from embryonic trabeculae are overrepresented in regenerated regions after a neonatal MI.**

(a) Left lateral view of hearts 2 or 21 days after neonatal MI as a validation of the surgical procedure. The position of the ligation is visible on the Connexin40-GFP-expressing coronary artery.

(b) Definition of the regenerated area. Transverse sections of infarcted hearts taken at three levels (i, ii, iii) from the ligation site to the apex, 2 and 21 days after a neonatal MI. Infarcted area are identified by a CD45 labeling of infiltrated immune cells at 2dpi and indicated by dotted lines while the thin remaining scar is identified by WGA staining at 21dpi. In green, Cx40-GFP and Cntn2 label the developing and mature PF network respectively. The region of interest (red line), including regenerated myocardium, is chosen around the remaining scar, covering the entire myocardial wall thickness. Control region (white line) is symmetrical to the region of interest in the unaffected region.

(c) Experimental workflow. Specific expression of Cx40-Cre in embryonic trabeculae (blue) leads to a mosaic genetic labelling (green) following tamoxifen injection at E14.5. At 21dpi, the infarcted area (red) is regenerated and labelled CMs, derived from embryonic trabeculae are overrepresented in regenerated regions (black line) in comparison to the control region (dotted line).

(d) Transverse sections of Sham- and MI-operated hearts 21 days after injury. The region of interest (ROI) is drawn in color and the control region in dotted grey.

(e) High magnification of the ROI after thresholding of the YFP signal. The myocardial wall is divided in 10 radial layers (thin lines and number) from endocardium to outer regions.

(f) Repartition of YFP positive CMs in the regenerated myocardium. The graph is expressed as a percentage of YFP area in each radial layer of the ROI, from subendocardial to outer regions, normalized by the total YFP area of control region, in MI (red curve) and sham (blue curve). Quantifications were conducted on serial sections below the ligation every 140µm (around 20 sections per hearts). Mean values are displayed, error bar: standard error SEM, Two-sided Wilcoxon's test. MI N= 15; Sham N= 11. P values are indicated in extended data Table 1.

RV: Right ventricle, LV: Left ventricle, ROI: Region of interest.

**Fig. 2: Cardiomyocytes derived from embryonic trabeculae enter cell cycle and express trabecular immature markers during the regeneration process.**

(a-c) Cell cycle activity is increased in embryonic-trabeculae derivatives during regeneration.

(a) Experimental workflow. Genetic labeling of embryonic derivatives is induced by tamoxifen injection at E14.5. EdU is injected at 5 and 11dpi, during the MI-induced proliferation wave.

(b) Transverse sections below the ligation showing YFP-positive CMs that derived from embryonic trabeculae, the WGA-positive remaining scar (left panel) and EdU+ nucleus (right panel). Arrows indicate YFP-EdU double-positive CMs.

(c) Percentage of YFP positive CMs that incorporate EdU during the assay. Box plots show the median, the 25th and 75th percentile, and the whiskers denote the minimum and maximum values at most 1.5 inter-quartile range of the hinge, respectively. Two-tailed Student's t-test, p-value=0,00064. MI N= 8; Sham N= 6

(d-f) Increased expression of the immature trabecular marker (Cx40) 4 days after neonatal MI.

(d) Experimental workflow.

(e) Cx40 is a dynamic marker of trabeculae during development. Immunolabelling of endogenous Cx40 protein at E14.5 and P0, maximum intensity projection of 10µm-thick stacks.

(f) Transverse sections below the ligation showing expression of Cx40-GFP at P5. Immunolabeling of Cx40-GFP (g) and endogenous Cx40 protein (h) in the infarcted region. Inset show endogenous Cx40 protein at high magnification near the endocardium (i) and at mid myocardium (j). Empty arrowheads show maturating PF, while white arrowheads show contractile CM with abnormal high Cx40 content. Maximum intensity projection of 15µm-thick stacks.

**Fig. 3: Persisting defects in the PF network of regenerated hearts.**
(a-e) The PF network is slightly damaged by the surgically induced MI and is incapable of regenerating
(a) Workflow*: Cx40-GFP* mice are used to study the damaged caused by the MI 1 to 3 days after the surgery, and the remaining damages after 21 days of regeneration.
(b) Open ventricles of MI-operated mice 2 and 21 days after MI. The PF network is visualized thanks to Cx40-GFP. Arrows point to a gap in the network at the ligation site.
(c) The percentage of damaged PF network is measured on successive sections from the base to the apex of the heart, and expressed as a proportion of damaged ventricular lumen (red) over the total ventricular lumen perimeter (green + red)
(d) Transverse sections at the site of the ligation, 2 and 21 days after MI. The PF network is shown in green with Cx40-GFP at 2dpi and Cntn2 at 21dpi. Infarcted territory (CD45) and remaining scar (WGA) are shown in red. Colored dotted lines delineate the healthy (green) and damaged (red) ventricular lumen.
(e) Comparison of the percentage of damaged PF network at T0 (T0 = 1 to 3dpi) and 21 days after the MI. Quantification were conducted on successive sections every 70µm (T0) and every 140µm (21dpi) from the base of the heart to the apex. MI N= 14; Sham N= 13. Box plots show the median, the 25th and 75th percentile, and the whiskers denote the minimum and maximum values, respectively. Two-sided Wilcoxon's test, p value = 0.64, black dot: mean, bold black line: median.
(f-i) The PF network that has matured in the BZ of the infarct is hyperplastic
(f) Increased PF network density after MI is visible on whole-mount open left ventricles thanks to Cntn2 and Cx40-GFP labeling, and on transverse sections (g) with Cntn2 labeling.
(h) Increased PF network volume after MI is quantified by Cntn2 positive area, on successive sections below the ligation (every 140µm, around 20 sections per heart), after normalization by the perimeter of the left ventricular lumen in corresponding section. Box plots show the median, the 25th and 75th percentile, and the whiskers denote the minimum and maximum values, respectively. Two-sided Wilcoxon's test, p-value=1,6 e-7. MI N= 19; Sham N= 17
(i) Increased number of PF counted as the number of Cntn2 positive cells, on one representative transverse section below the ligation, normalized by the perimeter of the left ventricular lumen in the corresponding section. Box plots show the median, the 25th and 75th percentile, and the whiskers denote the minimum and maximum values at most 1.5 inter-quartile range of the hinge, respectively. Two-tailed Student's t-test, p-value= 0,00025. MI N= 13; Sham N= 10
LV: Left ventricle, PM: papillary muscles.

**Fig. 4: The hyperplastic PF network of regenerated hearts has an intermediate phenotype between contractile myocardium and healthy PF network.**
(a) Workflow
(b) smFISH images on transverse sections from sham and MI hearts at 21dpi. Transcripts 8 well-described PF-enriched genes are displayed. Each dot represents one transcript. The PF network is easily detected in the sham by the high density of transcripts and hardly distinguishable from the working myocardium in the MI with low density of transcripts. Number of mice: MI N= 3; Sham N= 3
(c) Density of transcripts from PF-enriched genes (transcripts per $mm^2$), detected by smFISH, was quantified in the contractile myocardium and PF network (*Cntn2*+) of Sham and MI at 21dpi. Note the intermediate phenotype of MI PF network, between contractile myocardium and healthy PF network. Box plots show the median, the 25th and 75th percentile, and the whiskers denote the minimum and maximum values, respectively. Normality was tested by Shapiro-Wilk test and rejected if p-value<0.01. Homoscedasticity was tested by F- test and rejected if p-value<0.01. Student-t-test was used when normality and homoscedasticity were validated. Else, in case of heteroscedasticity the Welch Two samples T-Test was used, and, in case of non-normality, the Wilcoxon Rank Test was used.
(d-e) Immunofluorescence (d) and RNAscope (e-f) of PF-enriched genes on serial sections from those used for the smFISH. Each section (b-d-e-f) are 10µm-thick, successive, and inset show the same area. Magenta lines delineate the PF-network scored as Cntn2+ (d), *Cx40-GFP*+ (e).

(g-i) Lack of the typical elongated shape of PF in the hyperplastic PF network.
(g) Genetic strategy to induce sparse cell labeling.
(h) Visualization of PF shape, in healthy (Sham) and hyperplastic PF network (MI), 21 day after surgery. Combination of Cntn2 (membranous labelling) and sparse cell labeling (RFP) allow for visualization of individual PF on whole-mount open ventricles in three-dimensions using Imaris software. MIP images of open left ventricle are displayed. For better display, all RFP-positive PFs which could be individualized on the 3D images were manually segmented and are displayed in false colors on the right panel.
(i) Decrease in the length to width ratio of PFs in the hyperplastic PF network. Box plots show the median, the 25th and 75th percentile, and the whiskers denote the minimum and maximum values at most 1.5 inter-quartile range of the hinge, respectively. Black dot: mean. Two-sided Wilcoxon's test, p-value<2,2e-16. Number of mice: MI N= 4; Sham N= 3, number of cells: MI n=347; Sham n=411
LV: Left ventricle, PM: papillary muscles.

**Figure 5: Perturbed electrical propagation in regenerated hearts**
(a) Workflow
(b-c) Heterogenous levels and disorganization of conductive adhesion molecules and fast conducting gap junctions in the hyperplastic PF network.
(a) Sections showing Cntn2 and endogenous Cx40 expression in healthy and hyperplastic PF network.
(b) Serial section from the same region showing Cx43 expression. In the right panel, whole-mount view of Cntn2 and Cx43 expression of healthy and hyperplastic PF network.
(d-f) Surface electrocardiogram uncover perturbed electrical conduction in regenerated ventricles.
(d) Surface electrocardiogram recording at 21dpi in lead II
(e) Decreased conduction velocity in ventricles of regenerated hearts at 21dpi compared with healthy hearts as evidenced by the prolongation of the QRS interval in lead II. Box plots show the median, the 25th and 75th percentile, and the whiskers denote the minimum and maximum values at most 1.5 inter-quartile range of the hinge, respectively. Two-tailed Student's t-test, p-value=0,00016. MI N= 30; Sham N= 25
(f) Increased variability in the angle of the main activation axis at 21dpi. Mean +/- SD. MI N= 31; Sham N= 19
(g) Epicardial and endocardial optical mapping of regenerated hearts show no major defects in activation pattern.
For each heart, epicardial and endocardial activation maps are shown, overlay (transparency 50%) on the grayscale image. Activations maps of open ventricles were cropped to display only the activation of the endocardial surface. A confocal image of the same hearts, opened flat as for the endocardial mapping, shows the corresponding PF network.
Asterisks indicate the ligation site.

**Fig. 6: Hyperplasia of the PF network in response to MI depends on maximal level of Nkx2-5 following a recruitment mechanism.**
(a) Strategy 1 designed to test whether excessive PFs produced in response to MI arise from proliferation of preexisting PF. *Cx40-CreERT2::Rosa-YFP* mice are subjected to a neonatal MI, EdU is injected during the MI-induced proliferation wave (5 and 11dpi) and, three weeks after the surgery, EdU incorporation within the PF network of MI-operated mice is compared to that of Sham.
(b) Sections showing EdU incorporation in the Cntn2+ PF network. Arrows show EdU-positive PF nucleus.
(c) Comparison of the percentage of EdU positive PF nuclei between sham and MI. Box plots show the median, the 25th and 75th percentile, and the whiskers denote the minimum and maximum values at most 1.5 inter-quartile range of the hinge, respectively. Two-sided Wilcoxon's test, MI N= 6; Sham N= 7

(d) Strategy 2 designed to test whether excessive PFs produced in response to MI arise from excessive recruitment of new PFs. *Cx40-GFP; Nkx2-5* haploinsufficient mice are subjected to neonatal MI. PF network density and function are analyzed at 21dpi
(e) Cx40-GFP on wholemount open ventricles and Cntn2 on sections show hypoplastic PF network in both Sham and MI *Nkx2-5* haploinsufficient mice.
(f) The PF network of *Nkx2-5* haploinsufficient mice does not increased in volume after regeneration, thus remaining at its hypoplastic level. The PF network volume is quantified by Cntn2 positive area, on successive sections below the ligation (every 140µm, around 20 sections per heart), after normalization by the perimeter of the left ventricular lumen in corresponding section. Box plots show the median, the 25th and 75th percentile, and the whiskers denote the minimum and maximum values, respectively. Two-sided Wilcoxon's test, p-value: WT=3.5e-6, $Nkx2\text{-}5^{LacZ/+}$ =0,32. MI N= 13; Sham N= 12
(g) Surface electrocardiogram (lead II) shows that $Nkx2\text{-}5^{LacZ/+}$ mice have an increased QRS duration due to low Nkx2-5 dosage, with no additional conductive defects in response to MI. Box plots show the median, the 25th and 75th percentile, and the whiskers denote the minimum and maximum values at most 1.5 inter-quartile range of the hinge, respectively. Two-tailed Student's t-test, p-value: WT=0,00016, $Nkx2\text{-}5^{LacZ/+}$=0,54. MI N= 9; Sham N= 6
LV: Left ventricle, PM: papillary muscles.

**Fig. 7: Excessive PFs leading to PF network hyperplasia following MI are recruited from perinatal trabeculae**
(a) Workflow. Perinatal trabeculae are labelled by a 4'OH injection at E18.5 in *Cx40-CreERT2::R26R-TdTomato* mice. 21 days after a neonatal MI, the proportion of labelled PF within the apical PF network (hyperplastic region in MI) is compared to that of basal PF network (remote).
(b) Transverse sections showing cells derived from perinatal trabeculae in the healthy (Sham) or hyperplastic PF network (MI) in apical region.
(c) The hyperplastic PF network of MI operated mice is composed of a similar proportion of perinatal trabeculae than that of Sham. Because of variable recombination efficiency, the proportion of labelled PFs in the apical (hyperplastic) was compared to that of the basal (remote) PF network of the same animal, which thereby serves as an internal reference. Box plots show the median, the 25th and 75th percentile, and the whiskers denote the minimum and maximum values, respectively. Paired analysis (Two-sided Wilcoxon signed-rank by samples) shows no difference between apical and basal in neither Sham (p-value=0.06, N= 6) or MI (p-value=0.74, N=8).

**Fig. 8: Clonal analysis of Cx40-high expressing cells after cardiac regeneration**.
(a) Single cell labeling of the developing PF network is induced by the injection of a low dose of 4'OH tamoxifen at P1 in *Cx40-CreERT2::R26R-Confetti* mice. 21days after neonatal MI, the clone derived from this single cell is identified on WM. Number and phenotype (PF, Intermediate or CM) of cells in each clone are quantified on successive transverse section (every 20µm), and the clone is classified into one of the 3 categories (Conductive, mixed, contractile).
(b) Sections showing examples of clone belonging to each category depending on the Cntn2 expression level of the cell within the clone. The mixed clone category is composed of 4 subcategories: PF and CM; PF and intermediate; Intermediate and contractile, intermediate. Empty arrow: CM, white arrow: PF, arrow filled with grey: intermediate.
(c) Proportion of each clone category (contractile – mixed – conductive) expressed as a percentage of the total number of clones, in Sham and MI.
(d) Proportion of each subcategory of mixed clones expressed as a percentage of total number of clones, in Sham and MI.
(e) Number of cells per clone depending on the category of the clone (each dot represents a clone). Black dot: mean. Box plots show the median, the 25th and 75th percentile, and the whiskers denote

867 the minimum and maximum values at most 1.5 inter-quartile range of the hinge, respectively. Two-
868 sided Wilcoxon's test. P values are indicated in extended data Table 2a.
869 (f) Mean number of daughter cells derived from 100 mother cells, in Sham and MI, colored respective
870 to their cell type (PFs, Intermediate cells or CMs). This reflects fate choices and proliferation of the
871 initial labelled cell. Nmice: MI=6, Sham=5; nclones: MI=196, Sham= 138.
872

873
874

# Bibliography


1. Senyo, S. E. *et al.* Mammalian heart renewal by pre-existing cardiomyocytes. *Nature* **493**, 433–436 (2013).

2. Haissaguerre, M., Vigmond, E., Stuyvers, B., Hocini, M. & Bernus, O. Ventricular arrhythmias and the His-Purkinje system. *Nat. Rev. Cardiol.* **13**, 155–166 (2016).

3. Miquerol, L. *et al.* Biphasic development of the mammalian ventricular conduction system. *Circ. Res.* **107**, 153–161 (2010).

4. Miquerol, L. *et al.* Architectural and functional asymmetry of the His-Purkinje system of the murine heart. *Cardiovasc. Res.* **63**, 77–86 (2004).

5. Choquet, C., Kelly, R. G. & Miquerol, L. Nkx2-5 defines distinct scaffold and recruitment phases during formation of the murine cardiac Purkinje fiber network. *Nat. Commun.* **11**, 5300 (2020).

6. Delorme, B. *et al.* Developmental regulation of connexin 40 gene expression in mouse heart correlates with the differentiation of the conduction system. *Dev. Dyn.* **204**, 358–371 (1995).

7. Tian, X. *et al.* Identification of a hybrid myocardial zone in the mammalian heart after birth. *Nat. Commun.* **8**, 87 (2017).

8. Poss, K. D., Wilson, L. G. & Keating, M. T. Heart regeneration in zebrafish. *Science (80-. ).* **298**, 2188–2190 (2002).

9. Sedmera, D. & Thomas, P. S. Trabeculation in the embryonic heart. *BioEssays* **18**, 607–607 (1996).

10. Haubner, B. J. *et al.* Complete cardiac regeneration in a mouse model of myocardial infarction. **4**, 966–977 (2012).

11. Emde, B., Heinen, A., Gödecke, A. & Bottermann, K. Wheat germ agglutinin staining as a suitable method for detection and quantification of fibrosis in cardiac tissue after myocardial infarction. *Eur. J. Histochem.* **58**, 315–319 (2014).

12. Porrello, E. R. *et al.* Regulation of neonatal and adult mammalian heart regeneration by the miR-15 family. *Proc. Natl. Acad. Sci.* **110**, 187–192 (2013).

13. Wang, Z. *et al.* Mechanistic basis of neonatal heart regeneration revealed by transcriptome and histone modification profiling. *Proc. Natl. Acad. Sci. U. S. A.* **116**, 18455–18465 (2019).

14. Kretzschmar, K. *et al.* Profiling proliferative cells and their progeny in damaged murine hearts. *Proc. Natl. Acad. Sci. U. S. A.* **115**, E12245–E12254 (2018).

15. Pallante, B. A. *et al.* Contactin-2 Expression in the Cardiac Purkinje Fiber Network. *Circ. Arrhythmia Electrophysiol.* **3**, 186–194 (2010).

16. Gros, D. *et al.* Restricted distribution of connexin40, a gap junctional protein, in mammalian heart. *Circ. Res.* **74**, 839–851 (1994).

17. Kahr, P. C. *et al.* A novel transgenic Cre allele to label mouse cardiac conduction system: Cardiac conduction system mouse model. *Dev. Biol.* **478**, 163–172 (2021).

18. Shekhar, A. *et al.* Transcription factor ETV1 is essential for rapid conduction in the heart. *J. Clin. Invest.* **126**, 4444–4459 (2016).

19. Kim, K. H. *et al.* Irx3 is required for postnatal maturation of the mouse ventricular conduction

915 system. *Sci. Rep.* **6**, 1–14 (2016).

916 20. Goodyer, W. R. *et al.* Transcriptomic profiling of the developing cardiac conduction system at
917 single-cell resolution. *Circ. Res.* **125**, 379–397 (2019).

918 21. Delgado, C. *et al.* Neural cell adhesion molecule is required for ventricular conduction system
919 development. *Dev.* **148**, (2021).

920 22. van Eif, V. W. W., Stefanovic, S., Mohan, R. A. & Christoffels, V. M. Gradual differentiation and
921 confinement of the cardiac conduction system as indicated by marker gene expression.
922 *Biochim. Biophys. Acta - Mol. Cell Res.* **1867**, (2020).

923 23. Liang, X. *et al.* HCN4 dynamically marks the first heart field and conduction system precursors.
924 *Circ. Res.* **113**, 399–407 (2013).

925 24. Li, Y. *et al.* Genetic targeting of Purkinje fibres by Sema3a-CreERT2. *Sci. Rep.* **8**, 1–9 (2018).

926 25. Meysen, S. *et al.* Nkx2.5 cell-autonomous gene function is required for the postnatal
927 formation of the peripheral ventricular conduction system. *Dev. Biol.* **303**, 740–753 (2007).

928 26. Jay, P. Y. *et al.* Nkx2-5 mutation causes anatomic hypoplasia of the cardiac conduction system.
929 *J. Clin. Invest.* **113**, 1130–1137 (2004).

930 27. Sedmera, D. & Thompson, R. P. Myocyte proliferation in the developing heart. *Developmental*
931 *Dynamics* vol. 240 1322–1334 (2011).

932 28. de Boer, B. A., van den Berg, G., de Boer, P. A. J., Moorman, A. F. M. & Ruijter, J. M. Growth of
933 the developing mouse heart: An interactive qualitative and quantitative 3D atlas. *Dev. Biol.*
934 **368**, 203–213 (2012).

935 29. Challice, C. E. & Virágh, S. The architectural development of the early mammalian heart.
936 *Tissue Cell* **6**, 447–462 (1973).

937 30. Liu, X. *et al.* Cell proliferation fate mapping reveals regional cardiomyocyte cell-cycle activity
938 in subendocardial muscle of left ventricle. 1–16 (2021) doi:10.1038/s41467-021-25933-5.

939 31. Sánchez-Iranzo, H. *et al.* Tbx5a lineage tracing shows cardiomyocyte plasticity during zebrafish
940 heart regeneration. *Nat. Commun.* **9**, 428 (2018).

941 32. Cui, M. *et al.* Dynamic Transcriptional Responses to Injury of Regenerative and Non-
942 regenerative Cardiomyocytes Revealed by Single-Nucleus RNA Sequencing. *Dev. Cell* **53**, 102-
943 116.e8 (2020).

944 33. Cui, M. *et al.* Nrf1 promotes heart regeneration and repair by regulating proteostasis and
945 redox balance. *Nat. Commun.* **12**, 1–15 (2021).

946 34. Xiao, Q. *et al.* A p53-based genetic tracing system to follow postnatal cardiomyocyte
947 expansion in heart regeneration. *Dev.* **144**, 580–589 (2017).

948 35. Kimura, W. *et al.* Hypoxia fate mapping identifies cycling cardiomyocytes in the adult heart.
949 *Nature* **523**, 226–230 (2015).

950 36. Uva, G. D. *et al.* ERBB2 triggers mammalian heart regeneration by promoting cardiomyocyte
951 dedifferentiation and proliferation. **17**, (2015).

952 37. Konfino, T., Landa, N., Ben-Mordechai, T. & Leor, J. The type of injury dictates the mode of
953 repair in neonatal and adult heart. *J. Am. Heart Assoc.* **4**, e001320 (2015).

954 38. Gemberling, M., Karra, R., Dickson, A. L. & Poss, K. D. Nrg1 is an injury-induced cardiomyocyte

mitogen for the endogenous heart regeneration program in zebrafish. *Elife* **2015**, 1–17 (2015).

39. Zhao, L. *et al.* Notch signaling regulates cardiomyocyte proliferation during zebrafish heart regeneration. *Proc. Natl. Acad. Sci. U. S. A.* **111**, 1403–1408 (2014).

40. Honkoop, H. *et al.* Single-cell analysis uncovers that metabolic reprogramming by ErbB2 signaling is essential for cardiomyocyte proliferation in the regenerating heart. *Elife* **8**, 1–27 (2019).

41. Bersell, K., Arab, S., Haring, B. & Kühn, B. Neuregulin1/ErbB4 Signaling Induces Cardiomyocyte Proliferation and Repair of Heart Injury. *Cell* **138**, 257–270 (2009).

42. DeBenedittis, P. *et al.* Coupled myovascular expansion directs cardiac growth and regeneration. *Development* **149**, (2022).

43. Kikuchi, K. *et al.* Primary contribution to zebrafish heart regeneration by gata4+ cardiomyocytes. *Nature* **464**, 601–605 (2010).

44. van Duijvenboden, K. *et al.* Conserved NPPB+ Border Zone Switches From MEF2- to AP-1-Driven Gene Program. *Circulation* **140**, 864–879 (2019).

45. Sergeeva, I. A. *et al.* A transgenic mouse model for the simultaneous monitoring of ANF and BNP gene activity during heart development and disease. *Cardiovasc. Res.* **101**, 78–86 (2014).

46. Friedman, P. L., Stewart, J. R., Fenoglio, J. J. & Wit, A. L. Survival of subendocardial Purkinje fibers after extensive myocardial infarction in dogs. In vitro and in vivo correlations. *Circ. Res.* **33**, 597–611 (1973).

47. Garcia-Bustos, V. *et al.* Changes in the spatial distribution of the Purkinje network after acute myocardial infarction in the pig. *PLoS One* **14**, 1–17 (2019).

48. Wang, H. *et al.* Electrophysiologic Conservation of Epicardial Conduction Dynamics After Myocardial Infarction and Natural Heart Regeneration in Newborn Piglets. **9**, 1–10 (2022).

49. Watanabe, H. *et al.* Purkinje Cardiomyocytes of the Adult Ventricular Conduction System Are Highly Diploid but Not Uniquely Regenerative. *J. Cardiovasc. Dev. Dis.* **10**, 161 (2023).

50. Rentschler, S. *et al.* Myocardial notch signaling reprograms cardiomyocytes to a conduction-like phenotype. *Circulation* **126**, 1058–1066 (2012).

51. Darehzereshki, A. *et al.* Differential regenerative capacity of neonatal mouse hearts after cryoinjury. *Dev. Biol.* **399**, 91–99 (2015).

52. Haubner, B. J., Schuetz, T. & Penninger, J. M. A reproducible protocol for neonatal ischemic injury and cardiac regeneration in neonatal mice. *Basic Res. Cardiol.* **111**, 1–10 (2016).

53. Porrello, E. R. *et al.* Transient Regeneration Potential of the Neonatal Mouse Heart. *Science (80-. ).* **331**, 1078–1080 (2011).

54. Saker, D. M., Walsh-Sukys, M., Spector, M. & Zahka, K. G. Cardiac recovery and survival after neonatal myocardial infarction. *Pediatr. Cardiol.* **18**, 139–142 (1997).

55. Choquet, C. *et al.* Nkx2-5 Loss of Function in the His-Purkinje System Hampers Its Maturation and Leads to Mechanical Dysfunction. (2023).

56. Maury, P. *et al.* Cardiac Phenotype and Long-Term Follow-Up of Patients With Mutations in NKX2-5 Gene. *J. Am. Coll. Cardiol.* **68**, 2389–2390 (2016).

57. Logantha, S. J. R. J. *et al.* Remodeling of the Purkinje Network in Congestive Heart Failure in

995 the Rabbit. *Circ. Hear. Fail.* **14**, E007505 (2021).

996 58. Harris, B. S. *et al.* Remodeling of the peripheral cardiac conduction system in response to
997 pressure overload. *AJP Hear. Circ. Physiol.* **302**, H1712–H1725 (2012).

998 59. Blom, J. N., Lu, X., Arnold, P. & Feng, Q. Myocardial infarction in neonatal mice, a model of
999 cardiac regeneration. *J. Vis. Exp.* **2016**, 1–12 (2016).

1000 60. Beyer, S., Kelly, R. G. & Miquerol, L. Inducible Cx40-Cre expression in the cardiac conduction
1001 system and arterial endothelial cells. *Genesis* **49**, 83–91 (2011).

1002 61. Srinivas, S. *et al.* Cre reporter strains produced by targeted insertion of EYFP and ECFP into the
1003 ROSA26 locus. *BMC Dev. Biol.* **1**, 1–8 (2001).

1004 62. Madisen, L. *et al.* A robust and high-throughput Cre Repooting and characterization. *Nat*
1005 *Neurosci* **13**, 133–140 (2010).

1006 63. Snippert, H. J. *et al.* Intestinal crypt homeostasis results from neutral competition between
1007 symmetrically dividing Lgr5 stem cells. *Cell* **143**, 134–144 (2010).

1008 64. Saga, Y. *et al.* MesP1 is expressed in the heart precursor cells and required for the formation
1009 of a single heart tube. *Development* **126**, 3437–3447 (1999).

1010 65. Tanaka, M., Chen, Z., Bartunkova, S., Yamasaki, N. & Izumo, S. The cardiac homeobox gene
1011 Csx/Nkx2.5 lies genetically upstream of multiple genes essential for heart development.
1012 *Development* **126**, 1269–1280 (1999).

1013 66. Frankish, A. *et al.* GENCODE reference annotation for the human and mouse genomes. *Nucleic*
1014 *Acids Res.* **47**, D766–D773 (2019).

1015 67. Yates, A. D. *et al.* Ensembl 2020. *Nucleic Acids Res.* **48**, D682–D688 (2020).

1016 68. Marçais, G. & Kingsford, C. A fast, lock-free approach for efficient parallel counting of
1017 occurrences of k-mers. *Bioinformatics* **27**, 764–770 (2011).

1018 69. Gans, J. D. & Wolinsky, M. Improved assay-dependent searching of nucleic acid sequence
1019 databases. *Nucleic Acids Res.* **36**, 1–5 (2008).

1020 70. Rodriguez, J. M. *et al.* APPRIS 2017: Principal isoforms for multiple gene sets. *Nucleic Acids*
1021 *Res.* **46**, D213–D217 (2018).

1022 71. Bravo González-Blas, C. *et al.* SCENIC+: single-cell multiomic inference of enhancers and gene
1023 regulatory networks. *Nat. Methods* **20**, 1355–1367 (2023).

1024 72. De La Rosa, A. J. *et al.* Functional suppression of Kcnq1 leads to early sodium channel
1025 remodelling and cardiac conduction system dysmorphogenesis. *Cardiovasc. Res.* **98**, 504–514
1026 (2013).

1027 73. Kolesová, H., Olejníčková, V., Kvasilová, A., Gregorovičová, M. & Sedmera, D. Tissue clearing
1028 and imaging methods for cardiovascular development. *iScience* **24**, 1–25 (2021).

1029

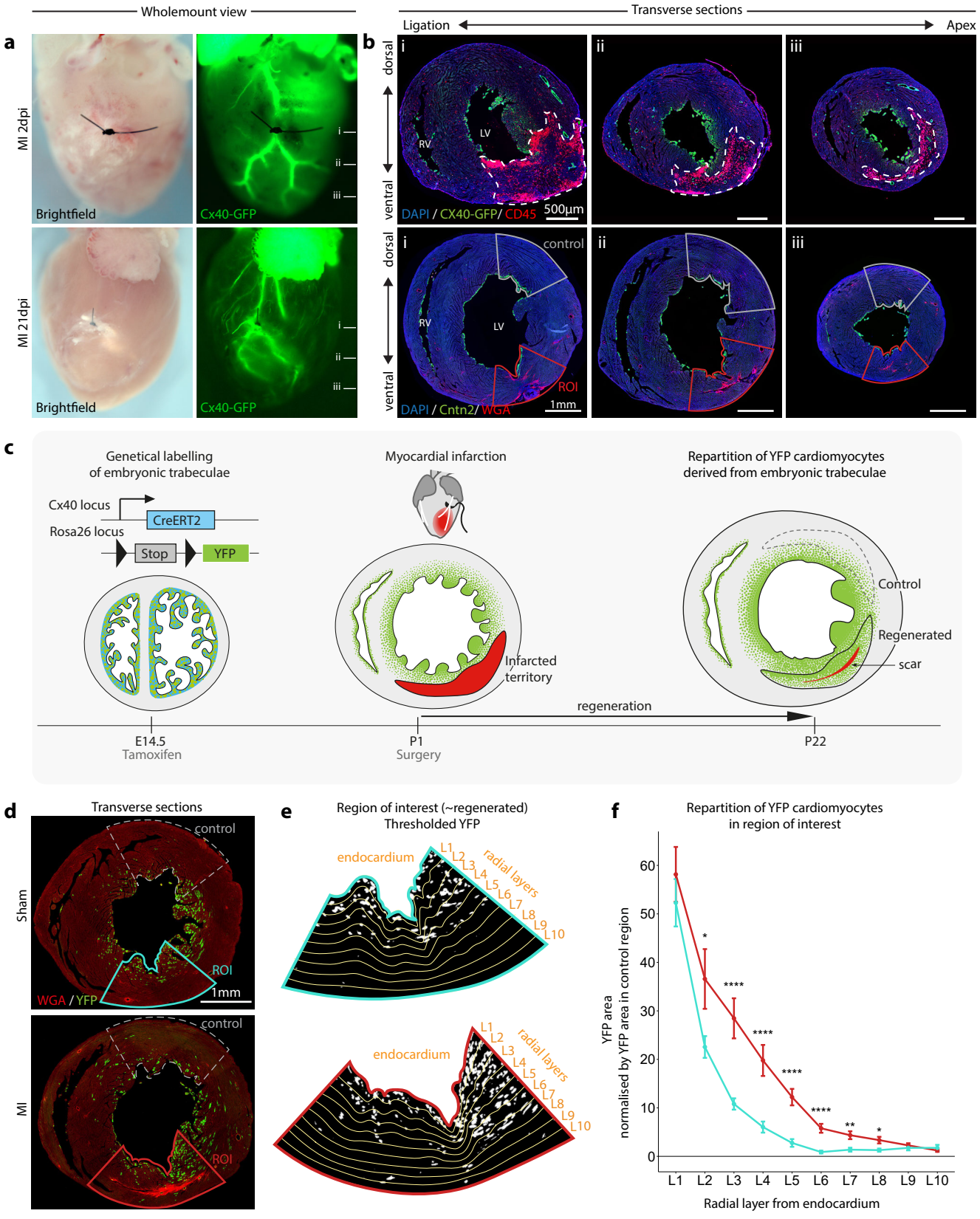
a
Wholemount view
MI 2dpi
MI 21dpi
Brightfield
Cx40-GFP
i
ii
iii
b
Transverse sections
Ligation
Apex
dorsal
ventral
RV
LV
DAPI / CX40-GFP/ CD45
500µm
control
ROI
DAPI / Cntn2/ WGA
1mm
c
Genetical labelling
of embryonic trabeculae
Cx40 locus
CreERT2
Rosa26 locus
Stop
YFP
Myocardial infarction
Infarcted
territory
Repartition of YFP cardiomyocytes
derived from embryonic trabeculae
Control
Regenerated
scar
regeneration
E14.5
Tamoxifen
P1
Surgery
P22
d
Transverse sections
Sham
MI
control
ROI
WGA / YFP
1mm
e
Region of interest (~regenerated)
Thresholded YFP
endocardium
radial layers
L1
L2
L3
L4
L5
L6
L7
L8
L9
L10
f
Repartition of YFP cardiomyocytes
in region of interest
YFP area
normalised by YFP area in control region
Radial layer from endocardium
*
****
**

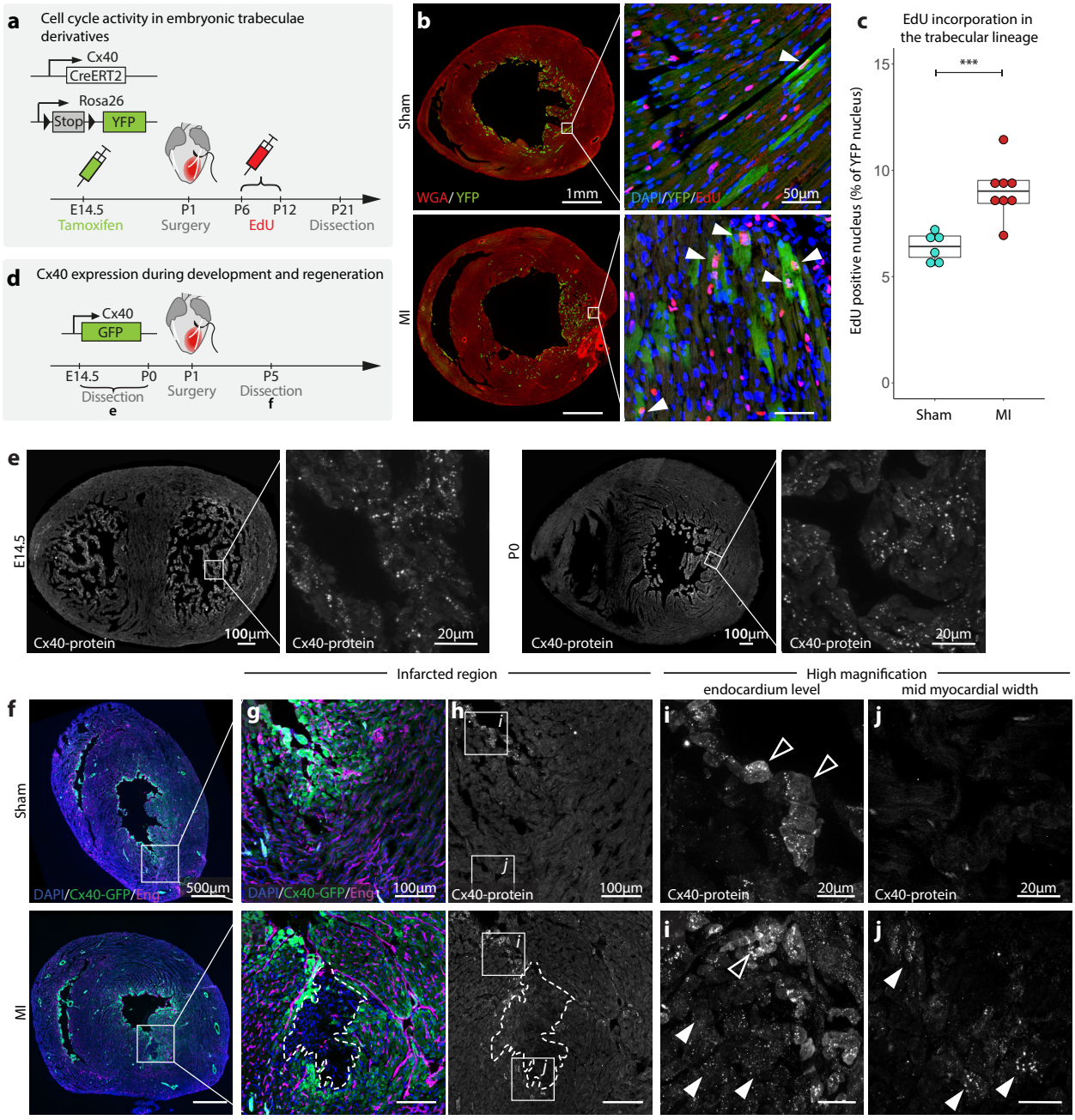
a
Cell cycle activity in embryonic trabeculae derivatives
Cx40
CreERT2
Rosa26
Stop
YFP
E14.5
Tamoxifen
P1
Surgery
P6
P12
EdU
P21
Dissection
b
Sham
MI
WGA/ YFP
1mm
DAPI/YFP/EdU
50µm
c
EdU incorporation in the trabecular lineage
EdU positive nucleus (% of YFP nucleus)
***
Sham
MI
d
Cx40 expression during development and regeneration
Cx40
GFP
E14.5
P0
Dissection
e
P1
Surgery
P5
Dissection
f
e
E14.5
P0
Cx40-protein
100µm
20µm
Infarcted region
High magnification
endocardium level
mid myocardial width
f
Sham
MI
DAPI/Cx40-GFP/Eng
500µm
100µm
Cx40-protein
20µm
g
h
i
j

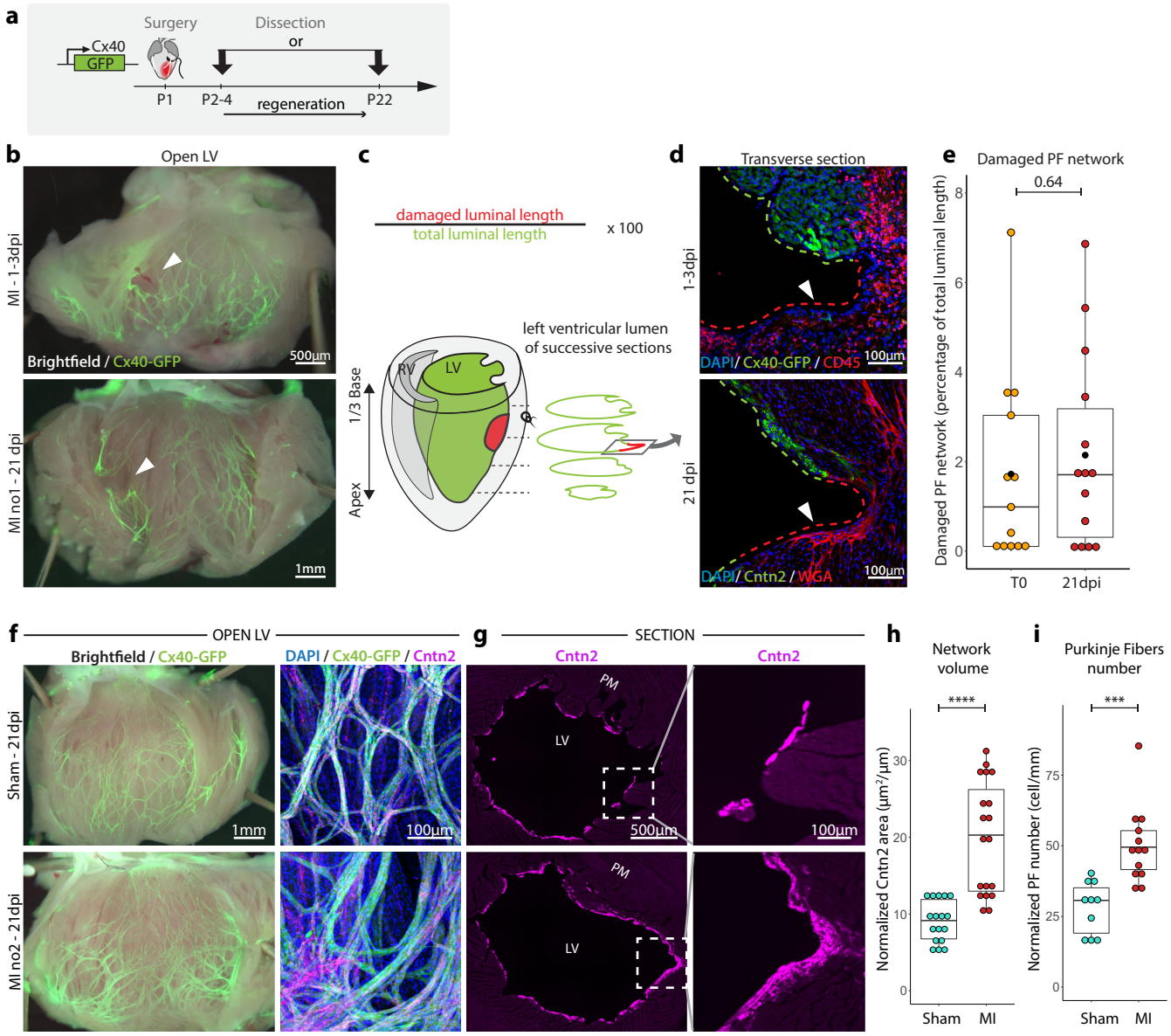
a
Surgery
Dissection
or
Cx40
GFP
P1
P2-4
regeneration
P22
b
Open LV
MI - 1-3dpi
Brightfield / Cx40-GFP
500µm
MI no1 - 21 dpi
1mm
c
damaged luminal length
total luminal length
x 100
left ventricular lumen
of successive sections
RV
LV
1/3 Base
Apex
d
Transverse section
1-3dpi
DAPI / Cx40-GFP / CD45
100µm
21 dpi
DAPI / Cntn2 / WGA
100µm
e
Damaged PF network
0.64
Damaged PF network (percentage of total luminal length)
T0
21dpi
f
OPEN LV
Brightfield / Cx40-GFP
DAPI / Cx40-GFP / Cntn2
Sham - 21dpi
1mm
100µm
MI no2 - 21dpi
g
SECTION
Cntn2
Cntn2
PM
LV
500µm
100µm
h
Network volume
****
Normalized Cntn2 area (µm²/µm)
Sham
MI
i
Purkinje Fibers number
***
Normalized PF number (cell/mm)
Sham
MI

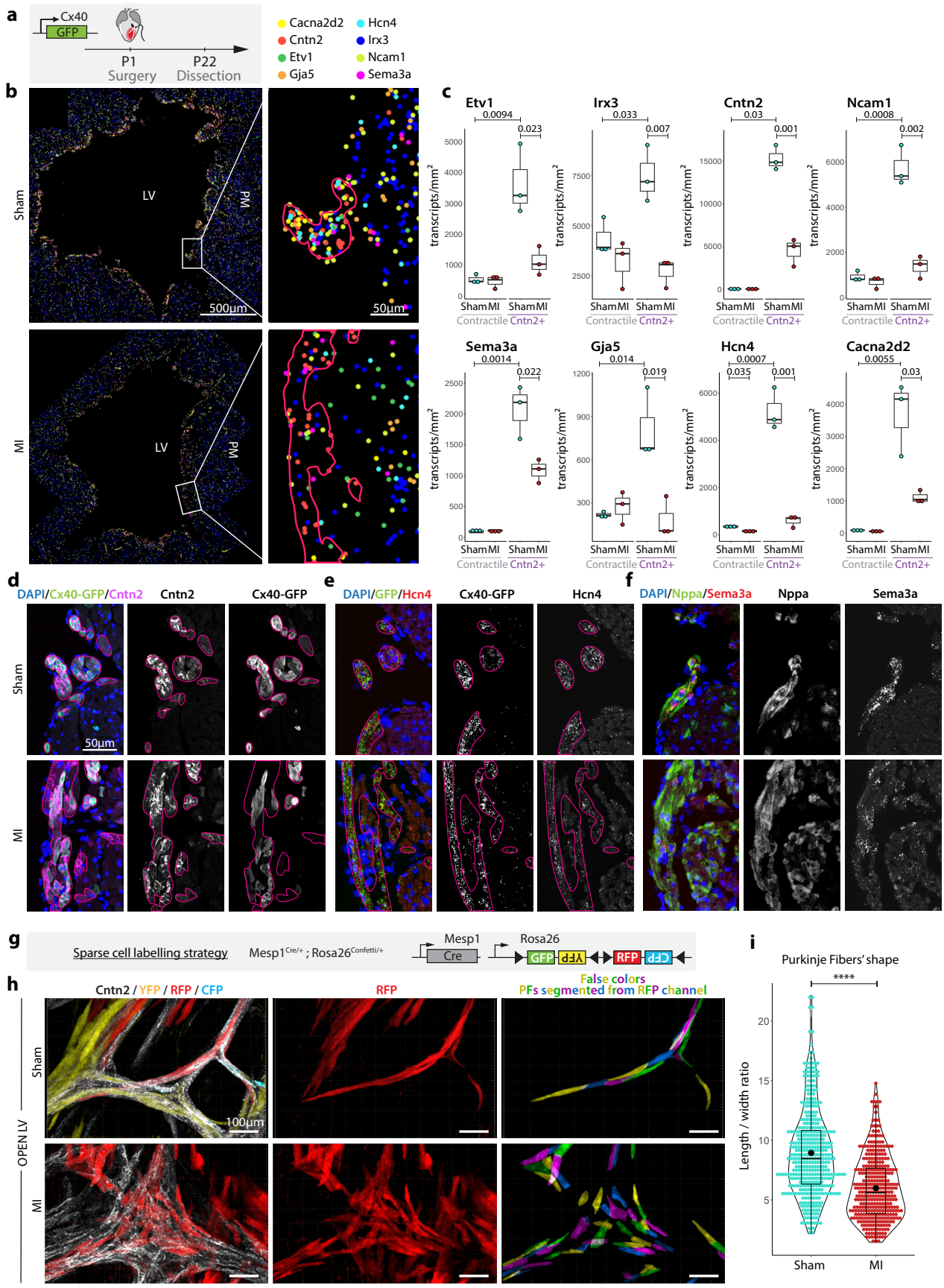
a
Cx40
GFP
P1
Surgery
P22
Dissection
Cacna2d2
Cntn2
Etv1
Gja5
Hcn4
Irx3
Ncam1
Sema3a
b
Sham
MI
LV
PM
500µm
50µm
c
Etv1
Irx3
Cntn2
Ncam1
Sema3a
Gja5
Hcn4
Cacna2d2
transcripts/mm²
Sham
MI
Contractile
Cntn2+
d
DAPI/Cx40-GFP/Cntn2
Cntn2
Cx40-GFP
e
DAPI/GFP/Hcn4
Cx40-GFP
Hcn4
f
DAPI/Nppa/Sema3a
Nppa
Sema3a
g
Sparse cell labelling strategy
Mesp1Cre/+ ; Rosa26Confetti/+
Mesp1
Cre
Rosa26
GFP
YFP
RFP
CFP
h
Cntn2 / YFP / RFP / CFP
RFP
False colors
PFs segmented from RFP channel
OPEN LV
100µm
i
Purkinje Fibers' shape
****
Length / width ratio
Sham
MI

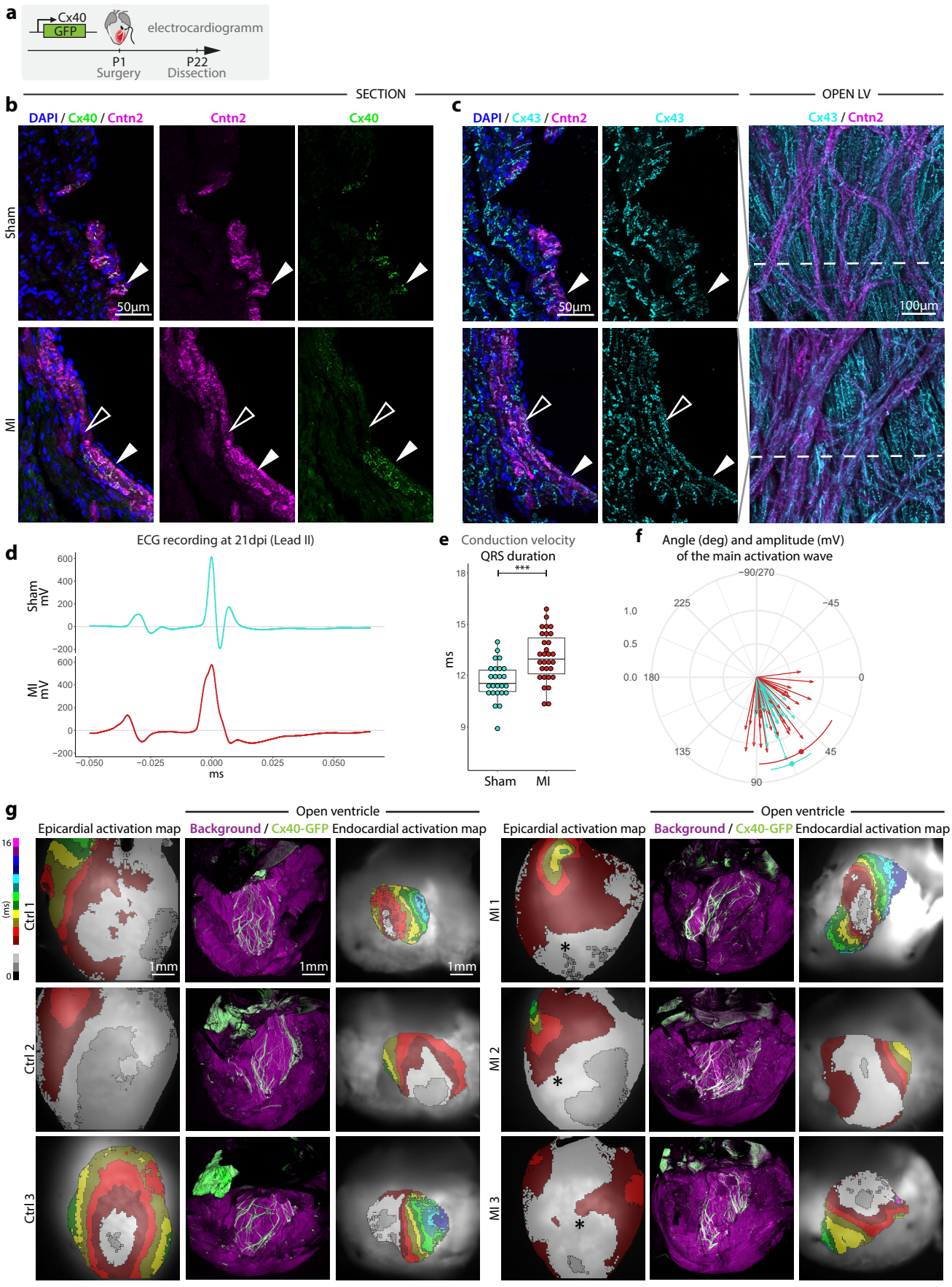
a
Cx40
GFP
electrocardiogramm
P1
Surgery
P22
Dissection
b
SECTION
DAPI / Cx40 / Cntn2
Cntn2
Cx40
Sham
MI
50µm
c
OPEN LV
DAPI / Cx43 / Cntn2
Cx43
Cx43 / Cntn2
50µm
100µm
d
ECG recording at 21dpi (Lead II)
Sham mV
MI mV
ms
e
Conduction velocity
QRS duration
***
ms
Sham
MI
f
Angle (deg) and amplitude (mV)
of the main activation wave
g
Open ventricle
Epicardial activation map
Background / Cx40-GFP
Endocardial activation map
Ctrl 1
Ctrl 2
Ctrl 3
MI 1
MI 2
MI 3
1mm

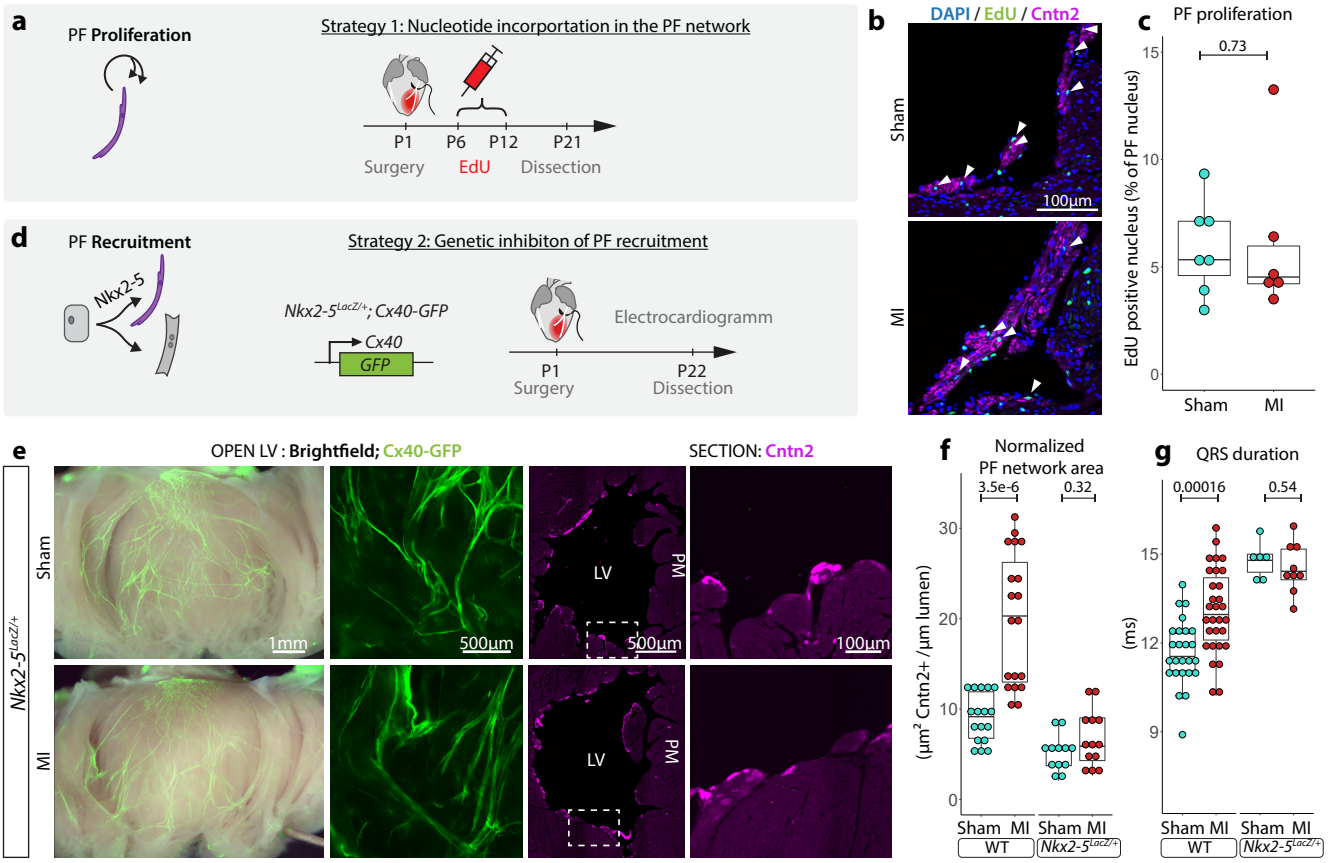
a
PF Proliferation
Strategy 1: Nucleotide incorportation in the PF network
P1
P6
P12
P21
Surgery
EdU
Dissection
b
DAPI / EdU / Cntn2
Sham
MI
100µm
c
PF proliferation
0.73
EdU positive nucleus (% of PF nucleus)
Sham
MI
d
PF Recruitment
Nkx2-5
Strategy 2: Genetic inhibiton of PF recruitment
Nkx2-5LacZ/+; Cx40-GFP
Cx40
GFP
Electrocardiogramm
P1
Surgery
P22
Dissection
e
OPEN LV : Brightfield; Cx40-GFP
SECTION: Cntn2
Nkx2-5LacZ/+
Sham
MI
1mm
500µm
LV
PM
100µm
f
Normalized
PF network area
3.5e-6
0.32
(µm² Cntn2+ /µm lumen)
Sham MI Sham MI
WT
Nkx2-5LacZ/+
g
QRS duration
0.00016
0.54
(ms)
Sham MI Sham MI
WT
Nkx2-5LacZ/+

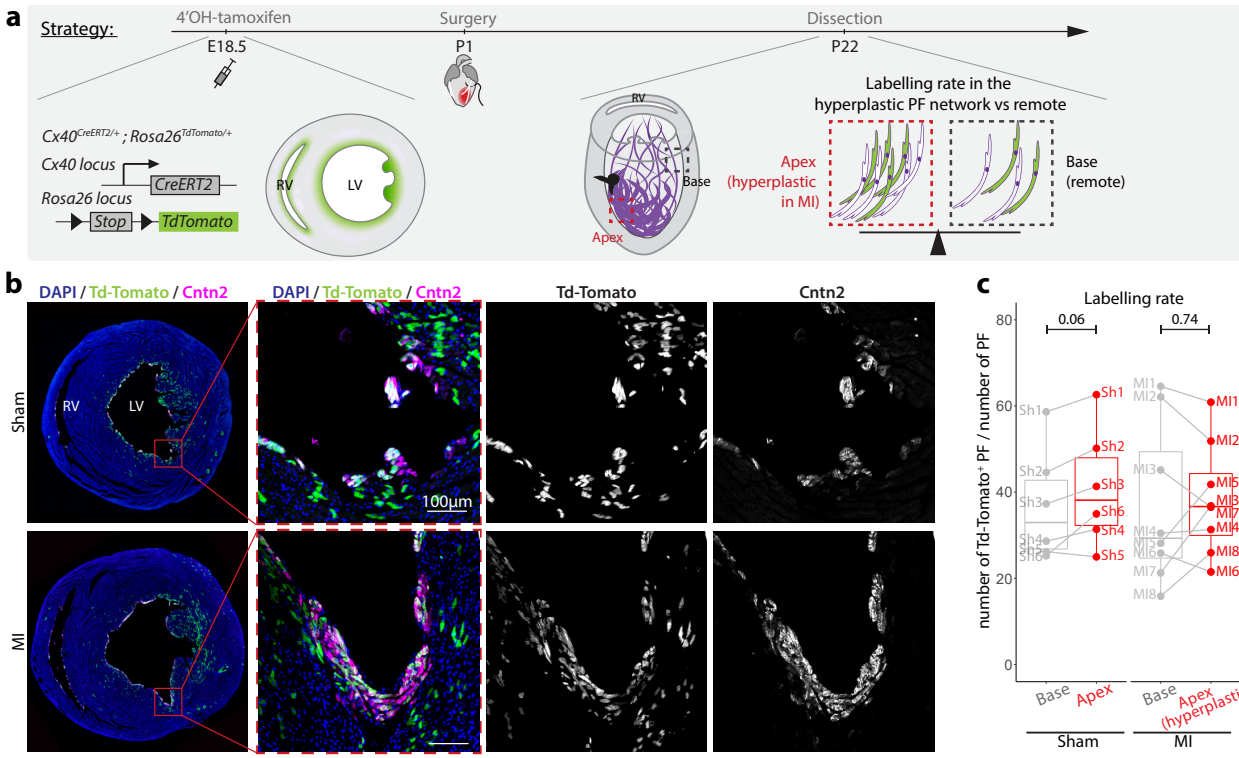
a
Strategy:
4'OH-tamoxifen
E18.5
Surgery
P1
Dissection
P22
Cx40CreERT2/+ ; Rosa26TdTomato/+
Cx40 locus
CreERT2
Rosa26 locus
Stop
TdTomato
RV
LV
Base
Apex
Labelling rate in the hyperplastic PF network vs remote
Apex (hyperplastic in MI)
Base (remote)
b
DAPI / Td-Tomato / Cntn2
DAPI / Td-Tomato / Cntn2
Td-Tomato
Cntn2
Sham
MI
RV
LV
100µm
c
Labelling rate
0.06
0.74
number of Td-Tomato+ PF / number of PF
Base
Apex
Base
Apex (hyperplastic)
Sham
MI

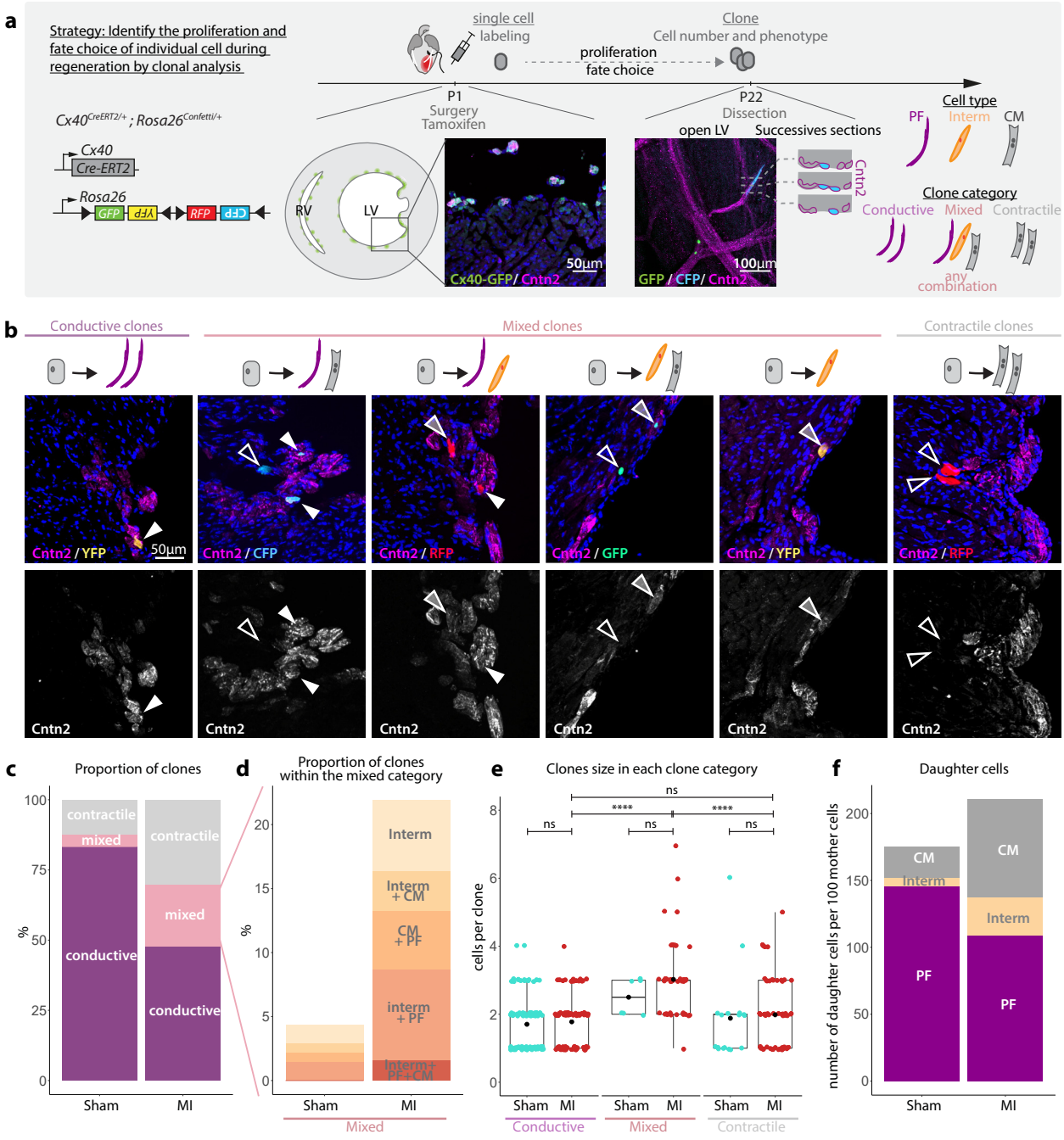
a
Strategy: Identify the proliferation and fate choice of individual cell during regeneration by clonal analysis
single cell labeling
Clone
Cell number and phenotype
proliferation
fate choice
P1
Surgery
Tamoxifen
P22
Dissection
open LV
Successives sections
Cell type
PF
Interm
CM
Clone category
Conductive
Mixed
Contractile
any combination
Cx40CreERT2/+ ; Rosa26Confetti/+
Cx40
Cre-ERT2
Rosa26
GFP
YFP
RFP
CFP
RV
LV
Cx40-GFP/ Cntn2
50µm
GFP / CFP/ Cntn2
100µm
Cntn2
b
Conductive clones
Mixed clones
Contractile clones
Cntn2 / YFP
50µm
Cntn2 / CFP
Cntn2 / RFP
Cntn2 / GFP
Cntn2 / YFP
Cntn2 / RFP
Cntn2
c
Proportion of clones
contractile
mixed
conductive
%
Sham
MI
d
Proportion of clones within the mixed category
Interm
Interm + CM
CM + PF
interm + PF
Interm+ PF+CM
Mixed
e
Clones size in each clone category
cells per clone
ns
****
Conductive
Mixed
Contractile
f
Daughter cells
number of daughter cells per 100 mother cells
CM
Interm
PF

| | Embryonic trabeculae (Tam E14.5) | | | | | Perinatal trabeculae (Tam E18.5) | | | | |
|---|---|---|---|---|---|---|---|---|---|---|
| layer | mean Sh (%) | mean MI (%) | p-value (wilcox-test) | significance | ratio | mean Sh (%) | mean MI (%) | p-value (wilcox-test) | significance | ratio |
| L1 | 52.3 | 58.1 | 0.6 | ns | _ | 62.3 | 77.8 | 0.02 | * | 1.2 |
| L2 | 22.5 | 36.6 | 0.02 | * | 1.6 | 11.0 | 19.6 | 0.05 | ns | _ |
| L3 | 10.8 | 28.5 | 0.00003 | **** | 2.6 | 3.8 | 11.7 | 0.04 | * | 3.1 |
| L4 | 6.0 | 19.8 | 0.00005 | **** | 3.3 | 1.1 | 7.3 | 0.002 | ** | 6.7 |
| L5 | 2.8 | 12.2 | 0.00004 | **** | 4.4 | 0.4 | 2.6 | 0.03 | * | 6.1 |
| L6 | 0.9 | 5.8 | 0.000005 | **** | 6.5 | 0.1 | 0.7 | 0.02 | * | 8.1 |
| L7 | 1.4 | 4.4 | 0.002 | ** | 3.2 | 0.1 | 0.3 | 0.2 | ns | _ |
| L8 | 1.3 | 3.3 | 0.013 | * | 2.6 | 0.0 | 0.1 | 0.7 | ns | _ |
| L9 | 1.7 | 2.3 | 0.4 | ns | _ | 0.1 | 0.1 | 0.7 | ns | _ |
| L10 | 1.8 | 1.2 | 0.8 | ns | _ | 0.3 | 0.1 | 0.6 | ns | _ |

**Extended Data Table 1: Repartition of genetically labelled CMs in regenerated myocardium.** Mean YFP or Tdtomato -labeled area in radial each layer of the ROI, from subendocardial (L1) to outer regions (L10), normalized by the total YFP-labeled area of control region, in MI and sham. P-value obtained from two tailed, unpaired T-Test.
MI N= 15; Sham N= 11 for lineage tracing induced at E14.5, Two-sided Wilcoxon's test.
MI N= 7; Sham N= 6 for lineage tracing induced at E18.5, Two-sided Wilcoxon's test.

**a**

| | proportion (%) | | | | Clone size | | | |
|---|---|---|---|---|---|---|---|---|
| clone category | Sh | MI | fold change | p-value MI vs Sham (wilcox) | Sh | MI | change (%) | p-value MI vs Sham (wilcox) |
| contractile | 11 | 30 | 2.7 | 0.004 (**) | 1.88 | 1.98 | 5.3 | 0.4 (ns) |
| mixed | 5 | 21 | 3.8 | 0.004 (**) | 2.50 | 3.23 | 29.3 | 0.27 (ns) |
| conductive | 83 | 49 | 0.6 | 0.008 (**) | 1.70 | 1.78 | 4.2 | 0.44 (ns) |

**b**

| | proportion (%) | | | | Clone size | | | |
|---|---|---|---|---|---|---|---|---|
| mixed clone sub-category | Sh | MI | fold change | p-value MI vs Sham (wilcox) | Sh | MI | change (%) | p-value MI vs Sham (wilcox) |
| Intermediate | 1.4 | 5.6 | 3.9 | 0.11 (ns) | 2.0 | 2.5 | 27.3 | 0.34 (ns) |
| Intermediate + CM | 0.7 | 3.1 | 4.2 | 0.34 (ns) | 3.0 | 3.0 | 0.0 | 0.79 (ns) |
| CM + PF | 0.7 | 4.6 | 6.3 | 0.1 (ns) | 3.0 | 3.8 | 25.9 | 0.72 (ns) |
| Intermediate + PF | 1.4 | 7.1 | 4.9 | 0.07 (ns) | 2.5 | 2.9 | 14.3 | 0.66 (ns) |
| Intermediate + CM+ PF | 0.0 | 1.5 | NA | 0.22 (ns) | 0 | 6.3 | NA | NA |

**c**

| | number of daughter cell per 100 mother cells | | | |
|---|---|---|---|---|
| Cell type | Sh | MI | change (%) | p-value MI vs Sham (wilcox) |
| CM | 23 | 73 | 217.39 | 0.004 (**) |
| intermediate | 6 | 28 | 366.67 | 0.02 (*) |
| PF | 145 | 109 | -24.83 | 0.009 (**) |
| total | 174 | 210 | 20.69 | 0.017 (*) |
| conductive (PF + intermediate) | 151 | 137 | -9.27 | 0.18 (ns) |

**Extended Data Table 2: Clonal analysis of Cx40 expressing cells at P1 after cardiac regeneration.**
(a) (left) Proportion of each clone category over the total number of clones in Sham and MI. (right) Number of cells per clone of each category. Two-sided Wilcoxon's test.
(b) (left) Proportion of each subcategory of mixed clones over the total number of clones. (right) Number of cells per clones of each subcategories. Two-sided Wilcoxon's test.
(c) Mean number of daughter cells derived from 100 mother cells, according to the type of the daughter cell (regardless of the clone category). This represent the mean number of daughter cells of each types, derived from a single Cx40-P1 cell.
Two-sided Wilcoxon's test. $\mathbf{N_{mice}}$: MI=6, Sh=5; $\mathbf{n_{clones}}$: MI=196, Sh= 138.

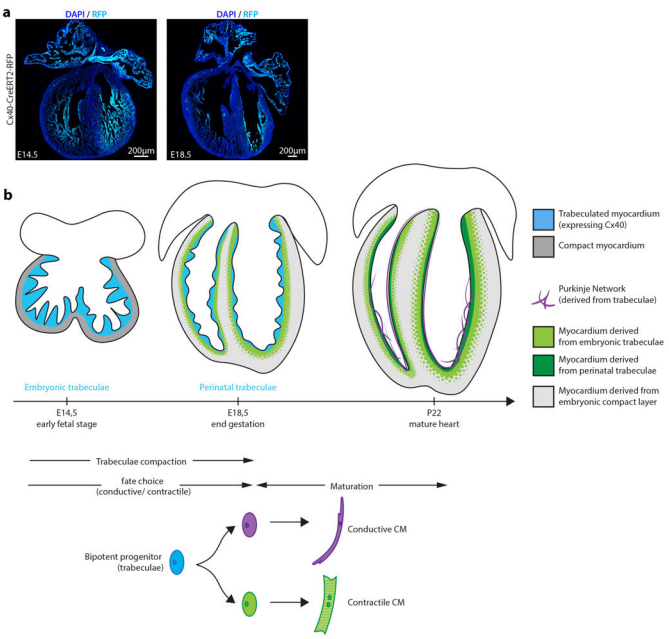


**Extended Data Fig. 1: Ventricular trabeculae during development and repartition of their derivatives in the mature heart.**

(a) Longitudinal sections of hearts from *Cx40-Cre-RFP* mice. Cx40 is expressed in the trabeculae, as seen by RFP expression, thus, genetic labeling in *Cx40-CreERT2* mice labels CM from the trabeculae.
(b) Cartoons summarizing the geometry of the trabeculae and the repartition of their derivatives at fetal, perinatal and mature stages. At E14.5, the trabeculae (cyan) reach their higher density. Thereafter, they progressively coalesce and give rise to subendocardial CMs (light green). Around birth, the innermost part of the embryonic trabeculae is not yet compacted, we call this area 'perinatal trabeculae'. The perinatal trabeculae give rise to the most subendocardial CMs (dark green) and to the PF network. The compact myocardium and its derivatives are shown in dark grey and grey, respectively. Concomitant with trabeculae compaction, bipotent progenitor from the trabeculae progressively segregate between conductive (purple) and contractile (green) fate. Final maturation extends until the third week of mice life.

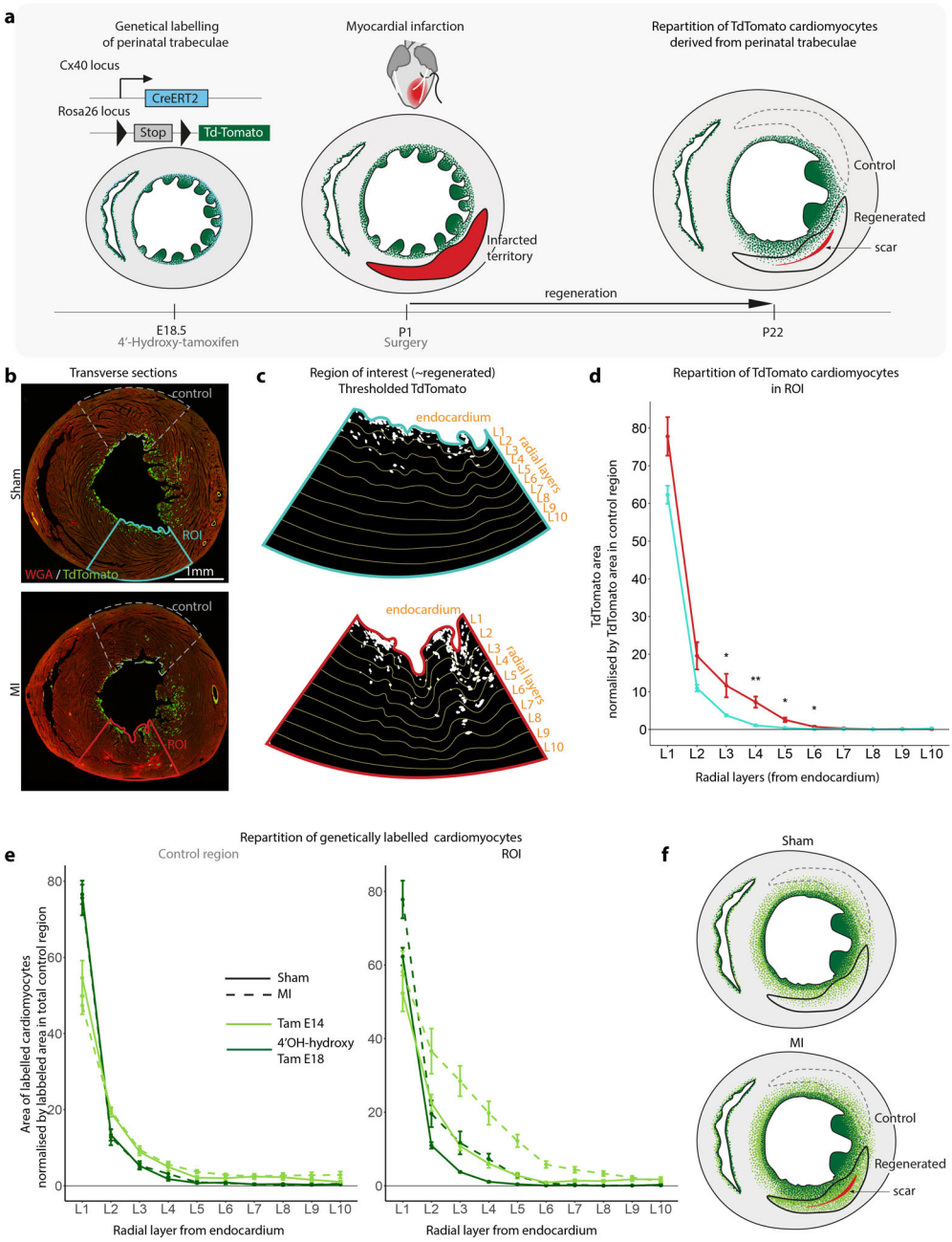


**Extended Data Fig. 2: Cardiomyocytes derived from perinatal trabeculae are overrepresented in regenerated regions following a neonatal MI.**

**(a)** Experimental workflow. Specific expression of Cx40-Cre in perinatal trabeculae (blue) leads to a mosaic genetic labelling (green) following a E18.5 4'-Hydroxy-tamoxifen injection. Infarcted area (red) is progressively regenerated, and labelled CMs derived from perinatal trabeculae are overrepresented in regenerated regions (black line) in comparison to the control region (dotted line).

**(b)** Transverse sections of Sham- and MI-operated hearts 21 days after injury. The region of interest (ROI) is drawn in color and the control region in dotted grey.

**(c)** High magnification of the ROI after thresholding of the TdTomato signal. Myocardial wall is divided in 10 radial layers (thin lines and number) from the endocardium (inner) to outer regions.

**(d)** Repartition of TdTomato positive CMs in the regenerated myocardium. The graph is expressed as a percentage of TdTomato area in each radial layer of the ROI, from subendocardial to outer regions, normalized by the total TdTomato area of control region, in MI (red curve) and sham (blue curve). Quantifications were conducted on serial sections bellow the ligation every 140µm (around20 sections per hearts). Mean values are displayed, error bar: standard error, Two-sided Wilcoxon's test. P values are indicated in extended data Table 1. MI N= 7; Sham N= 6.

**(e)** Comparison of the lineage tracing of embryonic trabeculae (E14), and perinatal trabeculae (E18). Area of genetically labelled CMs in each radial layer, from the endocardium to outer regions after an injection of tamoxifen at E14 (light green) or 4'-Hydroxy-tamoxifen at E18 (dark green), in Sham (full line) or MI (dotted line). The graph is expressed as a percentage of labeling in each radial layer of the control region (e) or ROI (e') and normalized by the total labeled area in control region. Mean values are displayed, error bar: standard error, Two-sided Wilcoxon's test. For embryonic trabeculae: MI N= 15; Sham N= 11. For perinatal trabeculae: MI N= 7; Sham N= 6.

**(f)** Cartoon summarizing the repartition on embryonic (light green) and perinatal (dark green) trabeculae in healthy and regenerated hearts.

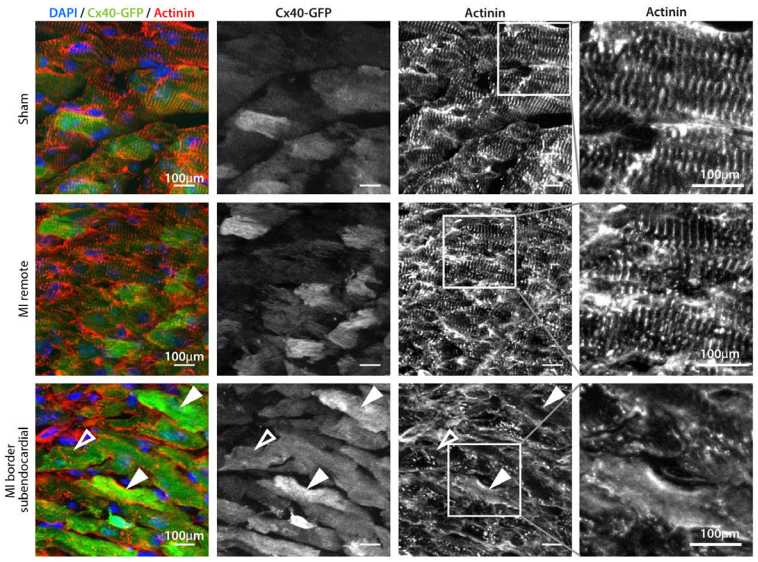


**Extended Data Fig. 3**: **Poor sarcomere assembly in the trabeculae-derived myocardium during regeneration**.
Actinin immunofluorescence show low (empty arrowhead) to null (white arrowhead) sarcomere assembly in Cx40-GFP-positive CMs from the subendocardial BZ at 5dpi in MI compared to Sham- operated mice.
Maximal intensity projection of 7.5µm-thick stacks.

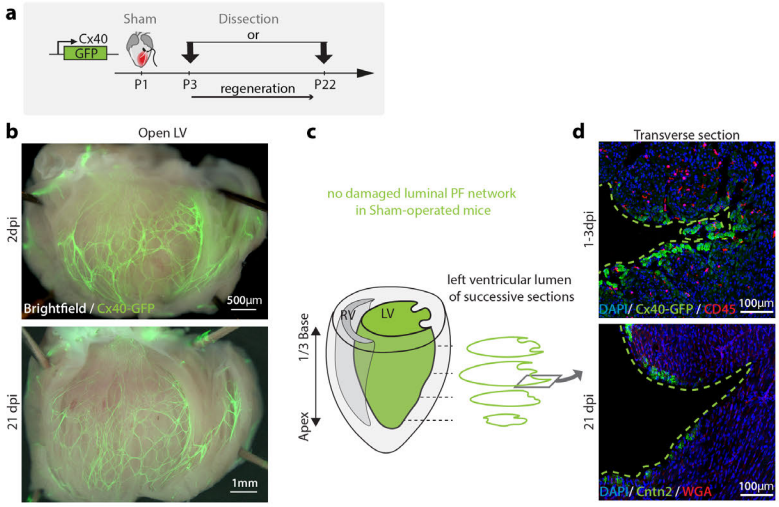


**Extended Data Fig. 4: No damage PF network observed in Sham-operated mice**
(a) Workflow*: Cx40-GFP* mice are used to study the damages caused by Sham surgery 1 to 3 days, or 21 days after surgery.
(b) Open ventricles of Sham-operated mice 2 and 21 days after surgery. The PF network is visualized thanks to Cx40-GFP.
(c) No damage of the PF network was observed at the luminal length at any level (successive transverse sections) in Sham-operated mice
(d) Transverse sections at 2 and 21 days after surgery. The PF network is shown in green with Cx40-GFP at 2dpi and Cntn2 at 21dpi. Although some infiltrated immune cells (CD45) are seen in the myocardium at 2dpi, no accumulation can be observed, and no loss of Cx40-GFP expression in subendocardial myocardium can be seen neither – contrary to MI-operated mice. At 21 post Sham-surgery, WGA staining can be observed in-between CMs, although no WGA rich area can be seen, contrary to MI-operated mice.

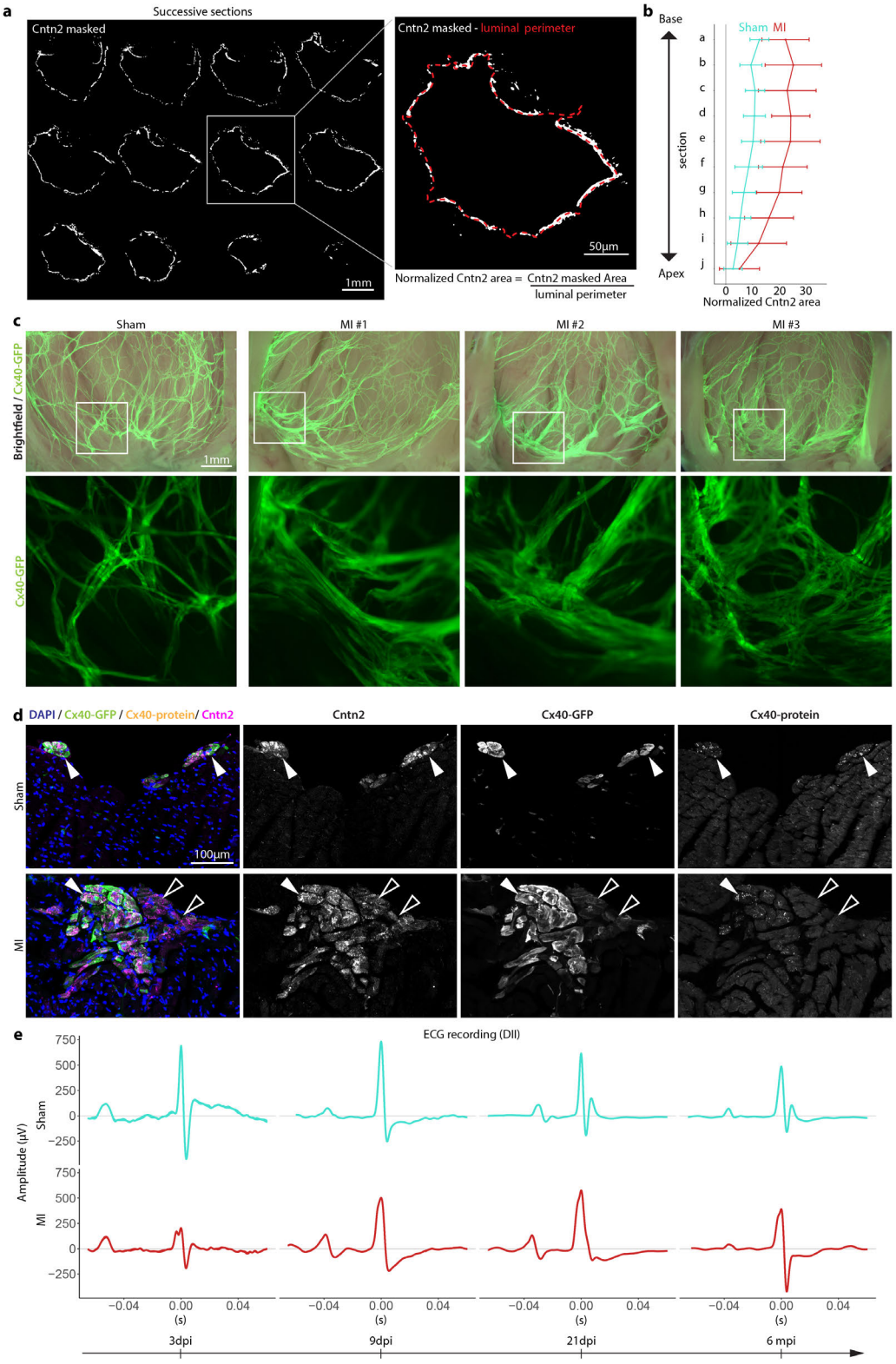


**Extended Data Fig. 5: Permanent hyperplasia of the PF network and functional defects**

(a) Cntn2 positive area is measured on successive transverse sections spaced 140µm apart. The ventricular lumen is delimitated automatically using the fluorescent background of the tissue at 21dpi. Cntn2 staining is thresholded after a gaussian blur of 2µm. The normalized Cntn2 area per section is expressed as the ratio of Cntn2 positive area divided by the luminal perimeter.

(b) Plot showing the normalized Cntn2 area along the apico-basal axis (a-j), in Sham (Bleu) and MI (Red) as measured in (a). MI N=19; Sh N=17 Error bars: standard deviation.

(c) Whole-mount open left ventricles six months after Sham or MI surgery in *Cx40-GFP* mice. Hyperplasia of the PF network is visible thanks to Cx40-GFP in all 3 MI.

(d) The intermediate phenotype in regenerated heats is permanent. Transverse sections of regenerated hearts 6 months post-injury show heterogenous expression of conductive adhesion molecules (Cntn2) and fast conducting gap junction (Cx40) in the hyperplastic PF network. White arrowheads: PFs, empty arrow heads: intermediate cells.

(e) Longitudinal study of cardiac conduction system function thanks to electrocardiogram recordings in leads II at 3dpi, 9dpi, 21dpi and 6 months post injury. Note the recovery of the QRS amplitude following myocardium regeneration, however,

ventricular conduction velocity remains slow as evidenced by prolonged QRS duration in MI compared to Sham at all stages. MI N=5; Sh N=5.

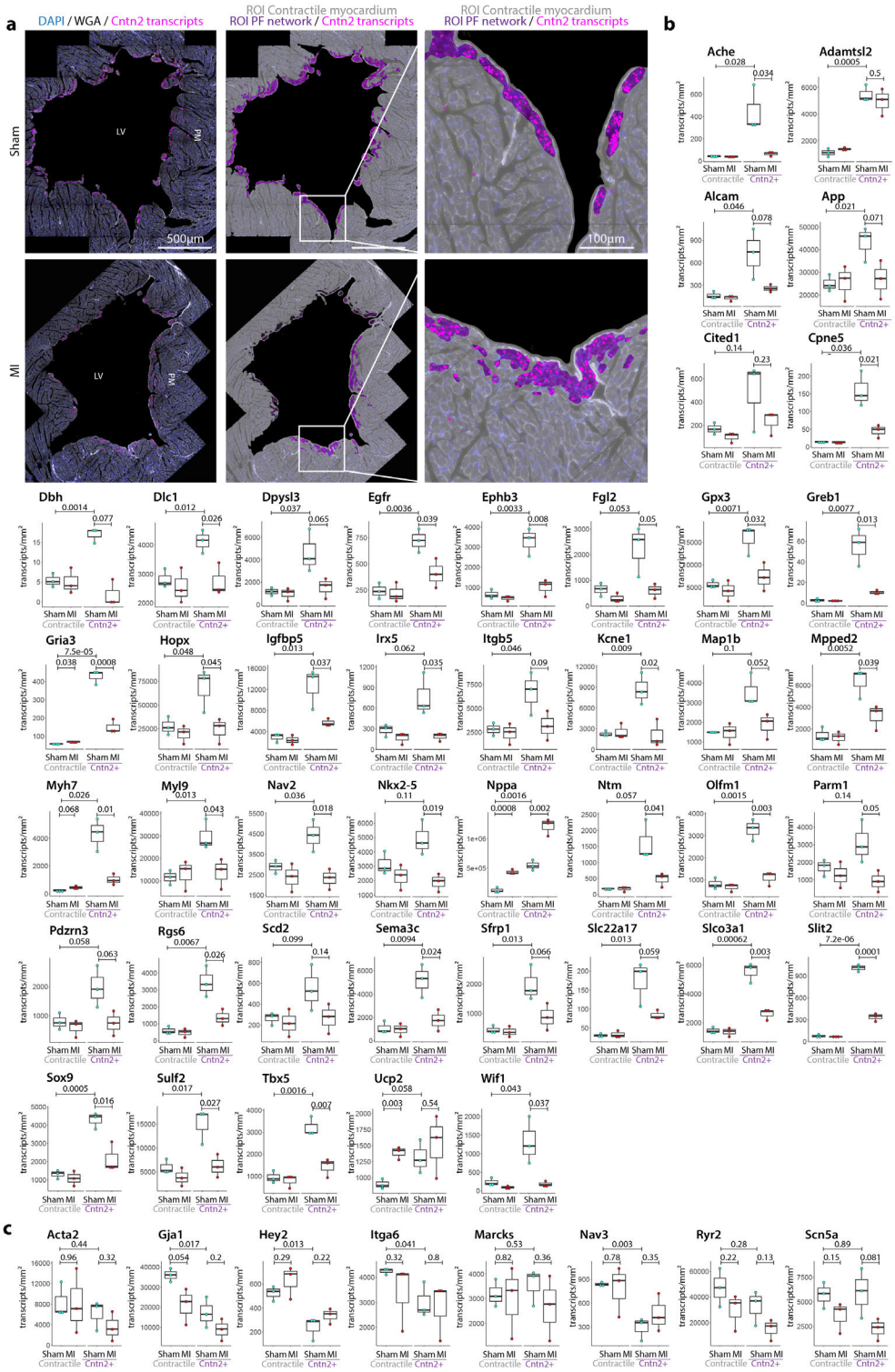


**Extended Data Fig 6: Downregulation of most PF-enriched genes in the hyperplastic PF-network of regenerated hearts.**

a) Transverse section of Sham and MI heart at 21dpi, processed with 100-plex smFISH. The PF network, ROI shown in purple, was delimited manually, including cells with Cntn2 transcripts (magenta dots). In the MI, only the PF network from the BZ of the infarct was analyzed. The contractile myocardium, ROI shown in gray, includes all the imaged tissue, except the PF region.

b) The density of RNA of each PF-enriched gene (transcripts per $mm^2$ of tissue), detected by smFISH, was quantified in the contractile myocardium and PF network of Sham and MI at 21dpi.

c) Density of transcripts from CM genes (transcripts per $mm^2$), detected by smFISH, was quantified in the contractile myocardium and PF network (Cntn2+) of Sham and MI at 21dpi.

N : Sham=3, MI=3. Box plots show the median, the 25th and 75th percentile, and the whiskers denote the minimum and maximum values, respectively. Normality was tested by Shapiro-Wilk test and rejected if p-value<0.01. Homoscedasticity was

tested by F- test and rejected if p-value<0.01. Two-sided Student-t-test was used when normality and homoscedasticity were validated. Else, in case of heteroscedasticity the Welch Two samples T-Test was used, and, in case of non-normality, the Two-sided Wilcoxon Rank Test was used. LV: Left ventricle, PM: papillary muscles, ROI, region of interest.

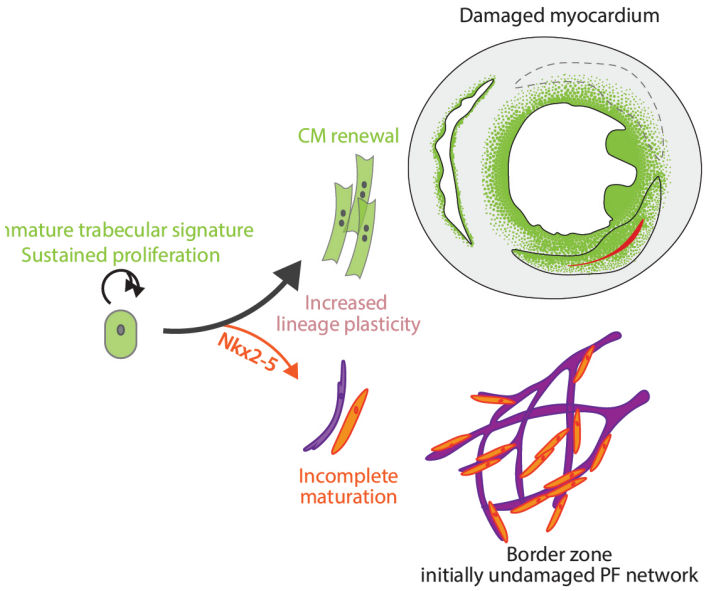


**Extended Data Fig. 7: Dual contribution of trabeculae during neonatal cardiac regeneration.**
Trabeculae participate in the regeneration of the contractile myocardium, and are thus found in increased proportions in regenerated myocardium. However, this contribution to the myocardium involves a perdurance of an immature phenotype in the trabeculae during regeneration which prolongs the plasticity between the contractile and conductive fates and results in ectopic conductive commitment. Excessive production of conductive cells is accompanied by incomplete conductive maturation producing a hyperplastic and immature PF network and resulting in altered ventricular conduction.